

# ICES REPORT 12-09

---

February 2012

## **in silico Vascular Modeling for Personalized Nanoparticle Delivery**

by

Shaolie S. Hossain, Yongjie Zhang, Xinghua Liang, Fazle Hussain, Mauro Ferrari, Thomas J. R. Hughes,  
Paolo Decuzzi



**The Institute for Computational Engineering and Sciences**  
The University of Texas at Austin  
Austin, Texas 78712

*Reference: Shaolie S. Hossain, Yongjie Zhang, Xinghua Liang, Fazle Hussain, Mauro Ferrari, Thomas J. R. Hughes, Paolo Decuzzi, in silico Vascular Modeling for Personalized Nanoparticle Delivery, ICES REPORT 12-09, The Institute for Computational Engineering and Sciences, The University of Texas at Austin, February 2012.*

| Report Documentation Page  |                                    |  | Form Approved<br>OMB No. 0704-0188                        |   |
|--|------------------------------------|--|---|---|
| Public reporting burden for the collection of information is estimated to average 1 hour per response, including the time for reviewing instructions, searching existing data sources, gathering and maintaining the data needed, and completing and reviewing the collection of information. Send comments regarding this burden estimate or any other aspect of this collection of information, including suggestions for reducing this burden, to Washington Headquarters Services, Directorate for Information Operations and Reports, 1215 Jefferson Davis Highway, Suite 1204, Arlington VA 22202-4302. Respondents should be aware that notwithstanding any other provision of law, no person shall be subject to a penalty for failing to comply with a collection of information if it does not display a currently valid OMB control number.   |                                    |  |   |   |
| 1. REPORT DATE<br><b>03 FEB 2012</b>   |                                    | 2. REPORT TYPE                           |   | 3. DATES COVERED<br><b>00-00-2012 to 00-00-2012</b> |
| 4. TITLE AND SUBTITLE<br><b>in silico Vascular Modeling for Personalized Nanoparticle Delivery</b>   |                                    | 5a. CONTRACT NUMBER                      |   |   |
|  |                                    | 5b. GRANT NUMBER                         |   |   |
|  |                                    | 5c. PROGRAM ELEMENT NUMBER               |   |   |
| 6. AUTHOR(S)   |                                    | 5d. PROJECT NUMBER                       |   |   |
|  |                                    | 5e. TASK NUMBER                          |   |   |
|  |                                    | 5f. WORK UNIT NUMBER                     |   |   |
| 7. PERFORMING ORGANIZATION NAME(S) AND ADDRESS(ES)<br><b>University of Texas at Austin, Institute for Computational Engineering and Sciences, Austin, TX, 78712</b>  |                                    | 8. PERFORMING ORGANIZATION REPORT NUMBER |   |   |
| 9. SPONSORING/MONITORING AGENCY NAME(S) AND ADDRESS(ES)  |                                    | 10. SPONSOR/MONITOR'S ACRONYM(S)         |   |   |
|  |                                    | 11. SPONSOR/MONITOR'S REPORT NUMBER(S)   |   |   |
| 12. DISTRIBUTION/AVAILABILITY STATEMENT<br><b>Approved for public release; distribution unlimited</b>  |                                    |  |   |   |
| 13. SUPPLEMENTARY NOTES  |                                    |  |   |   |
| 14. ABSTRACT<br><b>Drug biodistribution, bioavailability, efficacy and toxicity are unavoidably patientspecific. Here, computational models are utilized to predict the deposition of nanoparticles in a patient-specific arterial tree as a function of the vascular architecture flow conditions, receptor surface density, and nanoparticle properties. The Isogeometric Analysis framework, with an experimentally validated special boundary condition for the firm wall adhesion of nanoparticles, is used. The adhesion pattern correlates well with the spatial and temporal distribution of the wall shear rates. For the case considered, the larger (2.0 &amp;#956;m) particles adhere &amp;#8776; 2 times more in the lower branches of the arterial tree whereas the smaller (0.5 &amp;#956;m) particles deposit more in the upper branches. A change in patient-specific attributes, such as the branching angle and receptor density, dramatically affect particle adhesion. Our computational framework can be used to rationally select nanoparticle properties in conjunction with patient specific attributes to personalize, thus optimize, therapeutic interventions.</b> |                                    |  |   |   |
| 15. SUBJECT TERMS  |                                    |  |   |   |
| 16. SECURITY CLASSIFICATION OF:  |                                    |  | 17. LIMITATION OF ABSTRACT<br><b>Same as Report (SAR)</b> | 18. NUMBER OF PAGES<br><b>41</b>                    |
| a. REPORT<br><b>unclassified</b>   | b. ABSTRACT<br><b>unclassified</b> | c. THIS PAGE<br><b>unclassified</b>      |   |   |

# ***in silico* Vascular Modeling for Personalized Nanoparticle Delivery**

Shaolie S. Hossain, PhD<sup>1</sup>, Yongjie Zhang, PhD<sup>2</sup>, Xinghua Liang, MS<sup>2</sup>, Fazle Hussain, PhD<sup>3</sup>, Mauro Ferrari, PhD<sup>1</sup>, Thomas J. R. Hughes, PhD<sup>4</sup>, Paolo Decuzzi, PhD<sup>1,5\*</sup>

<sup>1</sup> Department of Translational Imaging, The Methodist Hospital Research Institute, Houston, TX

<sup>2</sup> Department of Mechanical Engineering, Carnegie Mellon University, Pittsburgh, PA

<sup>3</sup> Department of Mechanical Engineering, The University of Houston, Houston, TX

<sup>4</sup> Institute for Computational Engineering and Sciences, The University of Texas at Austin,  
Austin, TX

<sup>5</sup> Department of Experimental and Clinical Medicine, The University of Magna Graecia,  
Catanzaro, Italy

**Manuscript Submitted to Nanomedicine: Nanotechnology, Biology, and Medicine  
(JN201230)**

\* Corresponding author: Paolo Decuzzi, PhD; [PDecuzzi@tmhs.org](mailto:PDecuzzi@tmhs.org); The Methodist Hospital Research Institute, Department of Translational Imaging, 6670 Bertner Ave, Room R8-218, Houston (TX) 77030 – USA; phone: +1 713 441 7316; fax: + 1 713 441 7438

## **ABSTRACT**

Drug biodistribution, bioavailability, efficacy and toxicity are unavoidably patient-specific. Here, computational models are utilized to predict the deposition of nanoparticles in a patient-specific arterial tree as a function of the vascular architecture, flow conditions, receptor surface density, and nanoparticle properties. The Isogeometric Analysis framework, with an experimentally validated special boundary condition for the firm wall adhesion of nanoparticles, is used. The adhesion pattern correlates well with the spatial and temporal distribution of the wall shear rates. For the case considered, the larger (2.0  $\mu\text{m}$ ) particles adhere  $\approx 2$  times more in the lower branches of the arterial tree, whereas the smaller (0.5  $\mu\text{m}$ ) particles deposit more in the upper branches. A change in patient-specific attributes, such as the branching angle and receptor density, dramatically affect particle adhesion. Our computational framework can be used to rationally select nanoparticle properties in conjunction with patient specific attributes to personalize, thus optimize, therapeutic interventions.

Graphical Abstract: Figure 1

**KEY WORDS:** nanoparticles; rational design; mathematical modeling; vascular adhesion; personalized medicine

## BACKGROUND

It is well accepted that the outcome and safety of a therapeutic intervention is often affected by patient-specific attributes, at the gene, cell and organ levels <sup>1, 2</sup>. It is also increasingly recognized that results from clinical trials do not necessarily apply to individual patients, not even to the patients that were directly enrolled in the trials <sup>3</sup>. Every individual is shaped differently and the distribution, metabolism and elimination of drugs as well as their biochemical effects on the target cells are influenced by the patient age, genetic background and anatomical features. Computational modeling and nanomedicine are playing a major role in supporting the development of personalized therapeutic approaches <sup>4-8</sup>.

Computational modeling can capture the hierarchical complexity of biological systems and diseases over multiple scales – temporal and spatial – and include patient-specific information to personalize the outcome of the analysis. *in silico* modeling has been proven useful in orthopedic applications <sup>9, 10</sup>, for the treatment of cardiovascular diseases <sup>11-14</sup> and cancer <sup>15, 16</sup>, and in pharmacogenomic analysis <sup>6, 17</sup>. Segmental bone replacements can be optimally designed after a careful analysis of patient anatomical features and computation of the mechanical loads<sup>9</sup>. In cardiovascular diseases, the authentic geometry of the blood vessels and their mechanical properties have been incorporated in sophisticated computational tools to predict the distribution of wall shear stresses, risk of aneurysm rupture and to optimize the deployment of vascular stents <sup>18-20</sup>. Multi-physic models have been developed for predicting the response of tumors to molecular-based, radiation and thermal ablation therapies <sup>15, 16</sup>. Computational pharmacogenomics is used to predict *in silico* the efficacy, toxicity and possible resistance of drug molecules on different cell types <sup>6, 16</sup>.

On the other hand, a plethora of nanoparticle-based delivery systems have been developed over the last two decades for enhancing the tissue-specific accumulation of therapeutic molecules and the contrast generated by imaging agents. Indeed, the biodistribution and bioavailability of both therapeutic and imaging agents are dramatically affected by the *size, shape, surface* properties and mechanical *stiffness* (the

4Ss) of their carriers: the nanoparticles. This has been firstly predicted using mathematical models and then supported by experimental evidence, *in vitro* and *in vivo*<sup>21-23</sup>. Different fabrication strategies have been proposed to finely tune the geometrical, mechanical and surface properties of the nanoparticles<sup>24-27</sup>. But how such four parameters (*the 4Ss*) can be rationally exploited in conjunction with patient-specific attributes to personalize and, thus optimize, therapeutic interventions is still largely unexplored.

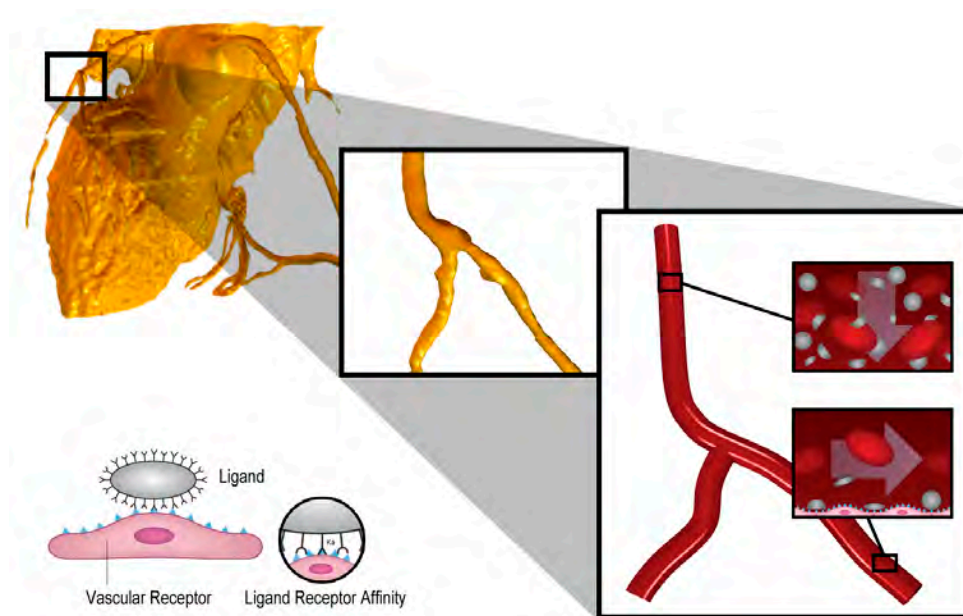


**Figure 1. Reconstructing the patient-specific vascular geometry.** The image shows, from left to right, the isocontour of a human heart, path extraction and editing of a small bifurcation portion from the left coronary artery (LCA) and reconstruction of the geometry ready for Isogeometric Analysis. Also, a nanoparticle with its ligand molecules is shown interacting with the receptor molecules decorating the surface of the endothelial cells in the vasculature.

Along this line, a patient-specific computational model is here presented for predicting the nanoparticle lodging within an authentic vascular network. Hexahedral solid NURBS (Non-Uniform Rational B-Splines) are used to accurately mesh the tridimensional architecture of an arterial tree, derived from the Computed Tomography (CT) scan of a patient<sup>28</sup>. The Finite Element Method (FEM), reformulated within the Isogeometric Analysis framework<sup>29</sup>, is employed to solve for the fluid and particle transport into the

authentic vasculature<sup>14</sup>. Information at the micro and nanoscale are introduced in the computational model by developing a special boundary condition at the vessel wall, accounting for cell/nanoparticle adhesion<sup>30</sup>. The model directly integrates information from the macroscale (vessel geometry and permeability, blood flow condition) with data pertaining to the micro and nanoscale (particle geometry, receptor density and affinity), thus avoiding massive, computationally inefficient discretization over multiple spatial and temporal scales. The proposed *in silico* model is first validated against *in vitro* parallel plate flow chamber experiments and then is applied for studying the effect of patient-specific attributes, such as the vascular geometry and receptor surface density, on the deposition of particles with different geometrical and surface properties within an authentic arterial tree.

## METHODS

**Reconstructing the patient-specific vascular geometry.** The input CT Angiography imaging data are often of poor quality due to large motions of the heart, as it supplies blood to the circulatory system. This makes it difficult to construct analysis-suitable patient-specific coronary models. To circumvent this problem, the raw imaging data were passed through a preprocessing pipeline where the image quality is improved by enhancing the contrast, filtering noise, classifying, and segmenting regions of interest<sup>28</sup>. A small bifurcation portion of the coronary tree was considered here including the left coronary artery (LCA), the left anterior descending artery (LAD) and the left circumflex artery (LCX) (Figure 1). The surface model of this bifurcation structure was extracted from the processed imaging data, and the vessel path was obtained after skeletonizing the volume bounded by the local luminal surface using Voronoi and Delaunay diagrams. The generated path can also be edited according to simulation requirements, e.g., extending the included branch angles to study how geometry such as the bifurcation angle influences particle delivery processes in coronary arteries. A skeleton-based sweeping method<sup>28</sup> was then used to generate hexahedral control meshes by sweeping a templated quadrilateral mesh of a circle along the arterial path. A template for the bifurcation configuration was used to decompose the geometry into three mapped meshable patches using the extracted skeleton. Each patch can be meshed using one-to-one sweeping

techniques. Some nodes in the control mesh lie on the surface, and some do not. We project nodes lying on the surface to the vascular surface. Finally, solid NURBS models were generated based on the constructed control meshes and they were employed in Isogeometric Analysis<sup>31,32</sup> to simulate blood flow and particle delivery in the coronary arteries.

**Governing equations for the fluid flow and particle transport.** A continuum-based approach was adopted to simulate blood flow and particle transport within a patient-specific vascular network (Figure 1). Blood was modeled as an incompressible Newtonian fluid with a density ( $\rho$ ) of 1060kg/m<sup>3</sup> and a dynamic viscosity ( $\mu$ ) of 0.003 N-s/m<sup>2</sup>, and the governing equations were formulated accordingly. Indeed, for sufficiently larger vessels (macrocirculation), the corpuscular component of blood (red blood cells, white blood cells and platelets) can be neglected and a Newtonian model for blood provides sufficiently accurate results<sup>33, 34</sup>. The strong form of the continuity and momentum balance equations in the fluid domain  $\Omega$  with its boundary  $\Gamma$  divided into three non-overlapping parts, the inflow ( $\Gamma_{in}$ ) and outflow ( $\Gamma_{out}$ ) boundaries and the vascular wall ( $\Gamma_s$ ), can be written as:

$$\rho \frac{\partial \mathbf{u}}{\partial t} + \rho \mathbf{u} \cdot \nabla \mathbf{u} + \nabla p - \nabla \cdot \mu (2 \nabla^s \mathbf{u}) = \mathbf{f} \quad \text{in } \Omega \times (0, T) \quad (1)$$

$$\nabla \cdot \mathbf{u} = 0 \quad \text{in } \Omega \times (0, T) \quad (2)$$

$$\mathbf{u} = \mathbf{g} \quad \text{on } \Gamma_{in} \times (0, T) \quad (3)$$

$$\mathbf{u} = \mathbf{0} \quad \text{on } \Gamma_s \times (0, T) \quad (4)$$

$$-p \mathbf{n} + \mu (2 \nabla^s \mathbf{u}) \cdot \mathbf{n} = \mathbf{0} \quad \text{on } \Gamma_{out} \times (0, T) \quad (5)$$

$$\mathbf{u}(\mathbf{x}, 0) = \mathbf{u}_0(\mathbf{x}) \quad \text{in } \Omega \quad (6)$$

where  $\mathbf{x}$  is a point in the spatial domain  $\Omega$  and  $t$  is a point in the time domain  $[0, T]$ . In these equations,  $\mathbf{u}(\mathbf{x}; t)$  represents the fluid velocity vector,  $p(\mathbf{x}; t)$  the pressure,  $\mathbf{f}$  the external body force,  $\mathbf{n}$  the unit outward normal to the surface, denoted  $\Gamma$ , and  $\mathbf{u}_0(\mathbf{x}; 0)$  the initial velocity vector. An inflow velocity vector  $\mathbf{g}(\mathbf{x}; t)$  was specified at the inlet ( $\Gamma_{in}$ ), a no-slip boundary condition (Eq.(4)) was prescribed at the rigid and impermeable vascular



wall ( $\Gamma_s$ ) and a stress free outflow boundary condition (Eq.(5)) was implemented at the branch outlets ( $\Gamma_{out}$ ).

The mass transport of the particles was assumed to be governed by a scalar advection-diffusion-reaction equation. This is a reasonable assumption for sufficiently small particles navigating in large vessels<sup>35,36</sup>. In the strong form, the transport problem can be stated as:

$$\frac{\partial C}{\partial t} + \mathbf{u} \cdot \nabla C - \nabla \cdot (\mathbf{K} \cdot \nabla C) + \sigma C = 0 \quad \text{in } \Omega \times (0, T) \quad (7)$$

$$C = C^0 \quad \text{on } \Gamma_{in} \times (0, T) \quad (8)$$

$$(\mathbf{K} \cdot \nabla C) \cdot \mathbf{n} = 0 \quad \text{on } \Gamma_{out} \times (0, T) \quad (9)$$

$$(\mathbf{K} \cdot \nabla C) \cdot \mathbf{n} + \Pi C = 0 \quad \text{on } \Gamma_s \times (0, T) \quad (10)$$

$$C(\mathbf{x}, 0) = 0 \quad \text{in } \Omega \quad (11)$$

where  $C(\mathbf{x};t)$  is the particle concentration,  $\mathbf{K}$  is the diffusivity tensor, and  $\sigma$  is the reaction coefficient. At the inlet (particle injection site)  $\Gamma_{in}$ , a Dirichlet boundary condition is prescribed (Eq. (8)) where  $C^0$  is the particle concentration given as:

$$\begin{aligned} C^0(\mathbf{x}, t) &= 1 \text{ for } 0 \leq t \leq t_i, \mathbf{x} \in \Gamma_{in} \\ C^0(\mathbf{x}, t) &= 0 \text{ for } t > t_i, \mathbf{x} \in \Gamma_{in} \end{aligned} \quad (12)$$

Here  $t_i$  denotes the duration of particle injection. At the outflow  $\Gamma_{out}$ , a homogenous Neumann boundary condition was specified (Eq.(9)); and a Robin-type boundary condition (Eq.(10)), a combination of the Dirichlet and Neumann conditions, was prescribed at the rigid wall interface ( $\Gamma_s$ ), where  $\Pi$  is defined in the sequel as the vascular deposition parameter.

Particle diffusivity was assumed to be isotropic and constant, and was determined from the Einstein-Stokes relation

$$D = \frac{k_B T}{3\mu d_p} \quad (13)$$

as a function of the particle size, where  $d_p$  is the diameter of the particles. Here  $k_B T$  represents the Boltzmann thermal energy. Then

$$\mathbf{K} = D\mathbf{I} \quad (14)$$

where  $\mathbf{I}$  is the  $3 \times 3$  identity matrix. The velocity field  $\mathbf{u}$  in Eq.(7) was obtained from the solution of the Navier–Stokes equations (Eqs.(1)-(6)) with the assumption that the flow physics affects the mass transport, not vice versa.

**Boundary condition for particle adhesion to the vessel wall.** The particle surface is assumed to be decorated with ligand molecules, uniformly distributed with a surface density  $m_l$ , that can specifically interact with counter molecules (receptors) expressed on the vessel wall with a surface density  $m_r$  (Figure 1). The molecular interaction between ligands and receptors is characterized by an affinity constant  $K_a^0$ , at zero mechanical load. From <sup>30</sup>, a probability of particle adhesion  $P_a$  can be derived as a function of its geometry (size and shape) and surface properties (ligand density, ligand type; surface electrostatic charge). The mathematical parameter  $P_a$  is defined as the probability of having at least one close ligand–receptor bond, and can be considered as a measurement of the strength of adhesion: the larger is  $P_a$ , the larger is the avidity and strength with which the particle firmly adheres to the wall. For a spherical particle of diameter  $d_p$ , the probability of adhesion can be expressed as follows <sup>30</sup>:

$$P_a \simeq m_r m_l K_a^0 \pi r_0^2 \exp \left[ -\frac{\lambda}{k_B T} \frac{6F^s \mu S}{m_r} \frac{d_p^2}{4r_0^2} \right] \quad (15)$$

where  $\lambda$  is a characteristic length of the ligand–receptor bond, generally of the order of 0.1 – 1 nm;  $k_B T$  is the Boltzmann thermal energy ( $= 4.142 \times 10^{-21}$  J);  $F^s$  is the coefficient of hydrodynamic drag force on the spherical particle;  $\mu S$  is the wall shear stress; and  $S$  is the wall shear rate. In Eq.(15), the parameter  $r_0$  is the radius of adhesion

$$r_0 = \frac{d_p}{2} \sqrt{\left[ 1 - \left( 1 - \frac{\Delta}{d_p/2} \right)^2 \right]} \quad (16)$$

with  $\Delta$  the separation distance between the particle and the substrate, at equilibrium. An alternative representation of Eq.(15) is,

$$P_a \simeq \alpha_1 \alpha_2 \pi r_0^2 \exp \left[ -\beta \frac{\mu S}{\alpha_2} \right] \quad (17)$$

where  $\alpha_1 = m_l K_a^0$  ( $= 0.023$ ) and  $\alpha_2 = m_r \left[ 1 - \left( 1 - \frac{\Delta}{d_p/2} \right)^2 \right]$  ( $\approx 1.369 \times 10^{10} \text{ \#}/\text{m}^2$  for  $d_p = 0.5 \text{ \mu m}$  and  $\approx 3.400 \times 10^9$  for  $d_p = 2 \text{ \mu m}$ ) are two governing parameters, and  $\beta = \frac{\lambda 6 F^s}{k_B T}$  ( $= 2.39 \times 10^{11} \text{ N}^{-1}$ ) is a constant. In Eq.(17),  $\alpha_1$ ,  $\alpha_2$ , the wall shear rate  $S$  and the particle diameter  $d_p$  are the independent governing parameters. For convenience,  $\lambda$  has been fixed to be 0.1 nm (see Table 1).

| Parameters                                     | Value   |
|--|---|
| Surface density of ligand molecules            | $m_l = 10^{15} \text{ \#}/\text{m}^2$           |
| Surface density of receptor molecules          | $m_r = 10^{13} \text{ \#}/\text{m}^2$           |
| Ligand-receptor affinity constant at zero load | $K_a^0 = 2.3 \times 10^{-7} \text{ m}^2$        |
| Characteristic length of ligand-receptor bond  | $\lambda = 1 \times 10^{-10} \text{ m}$         |
| Dynamic viscosity of water                     | $\mu = 0.001 \text{ N}\cdot\text{s}/\text{m}^2$ |
| Drag coefficient on the spherical particle     | $F^s = 1.668$                                   |

Table 1. Adhesion model parameters used.

The mass flux of particles ( $\partial C / \partial n$ ) in the direction  $\mathbf{n}$  normal to the wall can be related to the local increase in mass of particles adhering per unit surface  $\psi(\mathbf{x}; t)$  as

$$-(\mathbf{K} \cdot \nabla C) \cdot \mathbf{n}|_s = -D \frac{\partial C}{\partial n} \Big|_s = \frac{\partial \psi}{\partial t} \quad (18)$$

which simply derives from mass balance at the surface (accumulation of mass over time). Note that Eq.(18) is not a boundary condition yet, in that  $\psi(\mathbf{x}; t)$  is an unknown function. To close the system, an additional relation needs to be defined between  $\psi(\mathbf{x}; t)$  and  $C(\mathbf{x}; t)$ . The number of particles per unit surface  $\psi(\mathbf{x}; t)$  is in turn related to the volume concentration of particles at the wall through the equation

$$-D \frac{\partial C}{\partial n} \Big|_s = \frac{\partial \psi}{\partial t} = \Pi C|_s = P_a S \frac{d_p}{2} C|_s \quad (19)$$

Note that  $Sd_p/2$  is the fluid velocity in the center of a particle in proximity of the wall. The term  $\Pi = P_a Sd_p/2$  is called the vascular deposition parameter, in that the larger is  $\Pi$ , the larger is the number of particle adhering stably to the vessel walls under flow.

In the Supplementary Materials, the system of governing equations (1)-(19) is specialized to the case of a channel with a rectangular cross section simulating a parallel plate flow chamber, used for the *in vitro* validation of the proposed computational approach.

## RESULTS

**Predicting particle deposition in a parallel plate flow chamber apparatus.** The implementation of the boundary condition for particle adhesion was first validated against *in vitro* experiments conducted in a parallel plate flow chamber apparatus. A schematic of the system and the geometry used for the computational analysis are presented in Supplementary Figure 1. The particles are injected in a 20 mm long channel with a rectangular cross section ( $10 \times 0.274$  mm) under controlled hydrodynamic conditions (fixed wall shear rate  $S$ ). While the particles are transported downstream toward the waste, some of them can interact with and adhere firmly to the substrate. Details on the experimental conditions are provided in the Supplementary Materials.

The number of particles adhering  $n_{adh}$  per unit area  $A$ , normalized by the total number of injected particles  $n_{inj}$ , is presented in Figure 2 for different wall shear rates, namely  $S = 10, 75$  and  $200 \text{ s}^{-1}$ , and particle diameters. The experimental results (crosses with standard deviation bars) are compared with the numerical predictions (gray area), which are presented for different values of the parameters  $\alpha_1$  and  $\alpha_2$ , as utilized in Eq.(17). The gray areas are obtained for a  $\pm 5\%$  variation of the mean value of  $\alpha_1 (= 0.023)$  (Figure 2 – left column) and  $\alpha_2$  ( $\approx 9.44 \times 10^9$  for  $d_p \approx 0.7 \text{ }\mu\text{m}$ ;  $1.388 \times 10^9$  for  $d_p \approx 5 \text{ }\mu\text{m}$ ; and  $1.031 \times 10^9$  for  $d_p \approx 7 \text{ }\mu\text{m}$ ) (Figure 2 – right column).

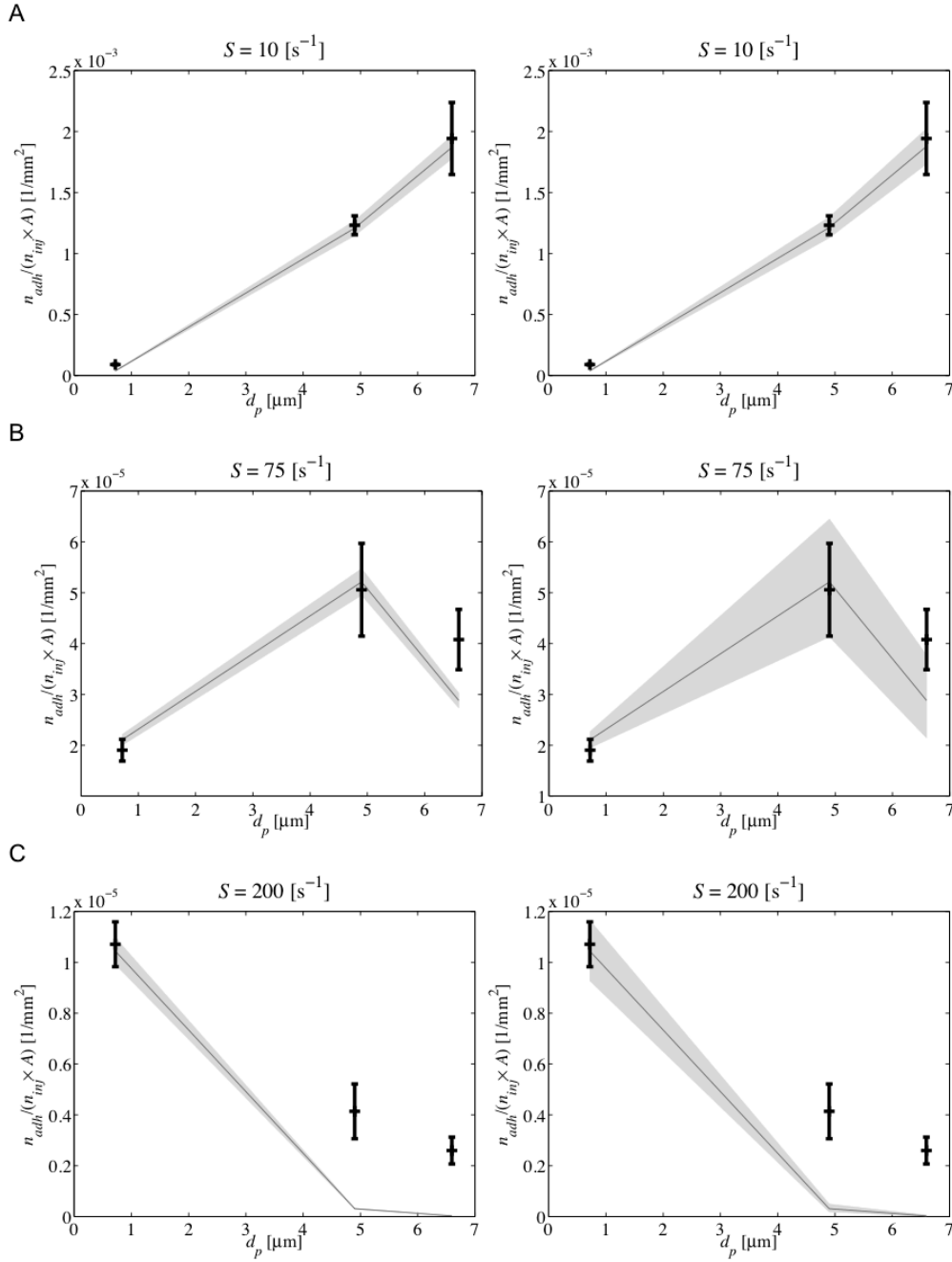


**Figure 2. Comparison between *in silico* and *in vitro* results.** The number of adhering particles  $n_{adh}$  per unit surface area  $A$  normalized by the total number of injected particles  $n_{inj}$  is plotted as a function of the particle diameter  $d_p$  and for three different wall shear rates: (A)  $S = 10 \text{ s}^{-1}$ , (B)  $S = 75 \text{ s}^{-1}$  and (C)  $S = 200 \text{ s}^{-1}$ . Black crosses with the standard deviation bars represent the experimental results obtained in a parallel plate flow chamber apparatus. The gray areas represent the *in silico* results obtained for values of the parameters  $\alpha_1$  (left) and  $\alpha_2$  (right) varying within  $\pm 5\%$  of their average values ( $\alpha_1 = 0.023$ ) and ( $\alpha_2 \approx 9.44 \times 10^9$  for  $d_p \approx 0.7 \text{ }\mu\text{m}$ ;  $1.388 \times 10^9$  for  $d_p \approx 5 \text{ }\mu\text{m}$ ; and  $1.031 \times 10^9$  for  $d_p \approx 7 \text{ }\mu\text{m}$ ).

Three different adhesive behaviors are depicted as a function of the wall shear rate  $S$ : i)  $n_{adh}$  grows steadily with  $d_p$ , for  $S = 10 \text{ s}^{-1}$  (Figure 2A); ii)  $n_{adh}$  grows, reaches a maximum and then decreases with  $d_p$ , for  $S = 75 \text{ s}^{-1}$  (Figure 2B); iii)  $n_{adh}$  decreases steadily with  $d_p$ ,  $S = 200 \text{ s}^{-1}$  (Figure 2C). Particle adhesion is determined by the balance between interfacial adhesive interactions (specific and non-specific) and the dislodging hydrodynamic forces. At low  $S$ , (Figure 2A) the former dominates the latter, thus the steady increase in  $n_{adh}$  up to  $d_p \approx 7 \text{ }\mu\text{m}$ . Conversely, at high  $S$ , the adhesive forces cannot balance the dislodging forces, and  $n_{adh}$  decreases steadily with  $d_p$  (Figure 2C). At intermediate values of  $S$ , a maximum in adhesion appears for an optimal particle diameter ( $\approx 5 \text{ }\mu\text{m}$ ). For the conditions analyzed here, this happens for  $d_p \approx 5 \text{ }\mu\text{m}$ , at  $S = 75 \text{ s}^{-1}$ . However, this maximum  $d_p$ , as well as its absolute value, changes with the adhesive properties of both the particle and the substrate<sup>30</sup>. Indeed, this maximum identifies the threshold in particle diameter below (above), which adhesive interactions prevail (do not prevail) over the dislodging hydrodynamic forces. Such a biphasic behavior was already predicted for the general case of oblate spheroidal particles as well<sup>30</sup>, and correlates with the dependence of the vascular deposition parameter  $\Pi$  on  $d_p$  (Supplementary Figure 2). Note that although the particles used in the flow chamber experiments were not decorated with any ligands, their adhesive behavior would follow the biphasic relationship of Eq.(17) due to the surface adsorption of non-specific molecules, mediating the interactions with the substrate.

Figure 2 demonstrates that the implemented adhesive boundary condition can accurately predict the complex, biphasic behavior for particle deposition under flow. Only at large shear rates,  $S = 200 \text{ s}^{-1}$ , and for large particle diameters ( $> 5 \text{ }\mu\text{m}$ ), the numerical predictions significantly underestimate the number of adhering particles. In this respect, however, it should be noted that for  $S = 200 \text{ s}^{-1}$  and  $d_p > 5 \text{ }\mu\text{m}$ , the absolute number of particles adhering is extremely small ( $\approx 2.5/\text{mm}^2$ ). Thus, both numerical and experimental inaccuracies could explain the observed discrepancy. It is also important to emphasize that due to the highly convective nature of the flow (Péclet number  $Pe \gg 1000$ ), there appears to be little or no effect of the particle size on near wall accumulation,

as shown in Supplementary Figure 3. This implies that particle deposition is governed by the vascular deposition parameter  $\Pi$ , under the condition considered here. Also, the surface density of the adhering particles does not vary significantly over the channel length, as demonstrated in Supplementary Figure 4.

**Predicting particle transport and deposition in a patient-specific vascular network.**

The Isogeometric Analysis formulation was used to simulate the transport and wall adhesion of particles injected through a catheter in a patient-specific arterial tree. From the CT scan imaging data of a healthy volunteer, a hexahedral solid NURBS model for a portion of the left coronary artery (LCA) tree was generated following the steps described in <sup>28</sup>. The geometry of the problem is presented in Figure 3A. A time-dependent pulsatile inflow condition <sup>37, 38</sup> with a period of 1 s (heart rate = 60 beats per minute) was imposed at the LCA inlet, where also a cylindrical catheter was located through which particles were injected, both radially and axially at a speed of 4 cm/s, for 5 cardiac cycles (5 s). The simulations were run on a computational mesh consisting of 55,100 quadratic NURBS elements for 14 cardiac cycles (14 s total) with a time step of 0.01 s employing the general solution strategies described in the Methods. Boundary layer meshes are used at the walls for more accurate computation of wall quantities, such as the wall shear rate.

The time evolution of the particle volumetric concentration within the vascular network is presented in Figures 3B-F. With time, the particle distribution front moves from the LCA inlet, where the catheter is located, toward the downstream branch and eventually into the side branches of the left anterior descending (LAD – left) and circumflex (LCX – right) artery. At 1 s, the particle front has passed the bifurcation (Figure 3C); at 5 s, the particles are uniformly distributed within the vascular tree (Figure 3D); and at 14 s, they have left the LCX and LAD (Figure 3F). This distribution was obtained for the 0.5  $\mu\text{m}$  particles.

In the sequel, the particle transport and wall deposition are analyzed as a function of the particle size and patient-specific attributes, such as the vascular geometry and the receptor surface density.

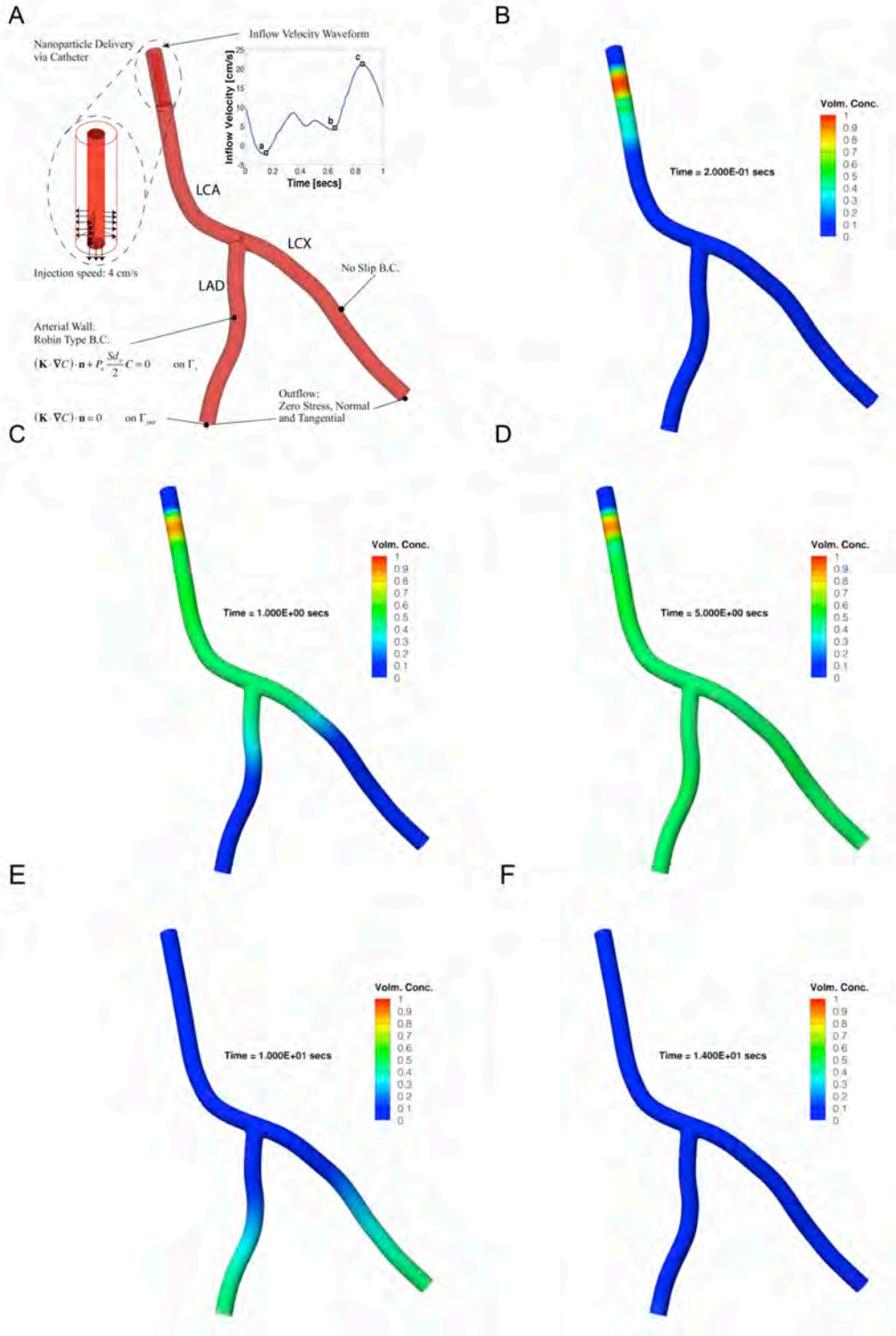


**Figure 3. Nanoparticle transport in a patient-specific vascular tree.** (A) Schematic of the coronary artery (branches identified) with the inlet velocity profile (inset at the right) and applied boundary conditions. (B)-(F) Volumetric concentration  $C$  of nanoparticles, normalized by the concentration at the catheter outlet  $C^0$ , at various times  $t$  post injection: (B)  $t = 0.2$  s, (C)  $t = 1$  s, (D)  $t = 5$  s, (E)  $t = 10$  s, and (F)  $t = 14$  s.



First, two particles with different diameters, namely  $d_p = 0.5$  and  $2 \mu\text{m}$ , were injected in the LCA. Figure 4 shows a side-by-side comparison of the time evolution for the wall surface concentration of the adhering particles, normalized by the injected dose. Three times are considered: 5, 10 and 14 s. For both particles, the surface concentration increases with time and becomes higher moving down the LCA, and approaching the LCX and LAD outlets. The larger particles ( $d_p = 2 \mu\text{m}$ ) exhibit about twice the adhesion of the smaller particles ( $d_p = 0.5 \mu\text{m}$ ), with a maximum normalized surface concentration of  $7 \times 10^{-8}$  and  $2 \times 10^{-8} \text{ cm}^{-2}$ , respectively. The smaller particles are observed to lodge more extensively in the upper branch (LCA) (Figure 4C).

As discussed in the previous section, particle adhesion is mostly governed by the vascular deposition parameter  $\Pi$  and the shear rate at the wall  $S$ . Therefore, the variation of  $S$  along the vascular tree and the flow conditions were carefully quantified over time, as shown in Supplementary Figure 5. In the LCA, large shear rates are computed within the first 5 cardiac cycles (i.e., continuous injection), with values of the order of  $500 - 1000 \text{ s}^{-1}$ , occurring in proximity of the branching point. Much lower values are computed in the LAD and LCX with  $S < 200 \text{ s}^{-1}$ . After 5 s, when the flow is no longer perturbed by the catheter injection, the wall shear rate decreases along the vascular tree with characteristic values ranging between  $300 - 400 \text{ s}^{-1}$  in the LCA and lower than  $100 \text{ s}^{-1}$  in the LAD and LCX. A comparison of Figure 4 and Supplementary Figure 5d reveals that the surface deposition patterns for the particles correlate well with the corresponding time averaged  $S$  distributions.

In the lower branches (LAD and LCX), before and after injection, the wall shear rate is generally equal to or lower than  $\approx 100 \text{ s}^{-1}$ . Within this  $S$  range, the vascular deposition parameter  $\Pi$  for the  $2 \mu\text{m}$  particles is, on the average, larger than that for the  $0.5 \mu\text{m}$  particles (Supplementary Figure 2: at  $S = 50 \text{ s}^{-1}$ ,  $\Pi \approx 3.5 \times 10^{-6} \text{ mm/s}$  for the  $2 \mu\text{m}$  particles,  $\Pi \approx 1.75 \times 10^{-6} \text{ mm/s}$  for the  $0.5 \mu\text{m}$  particles), thus explaining the larger adhesion ( $\approx 2$  times) of the former compared to the latter. On the other hand, for larger

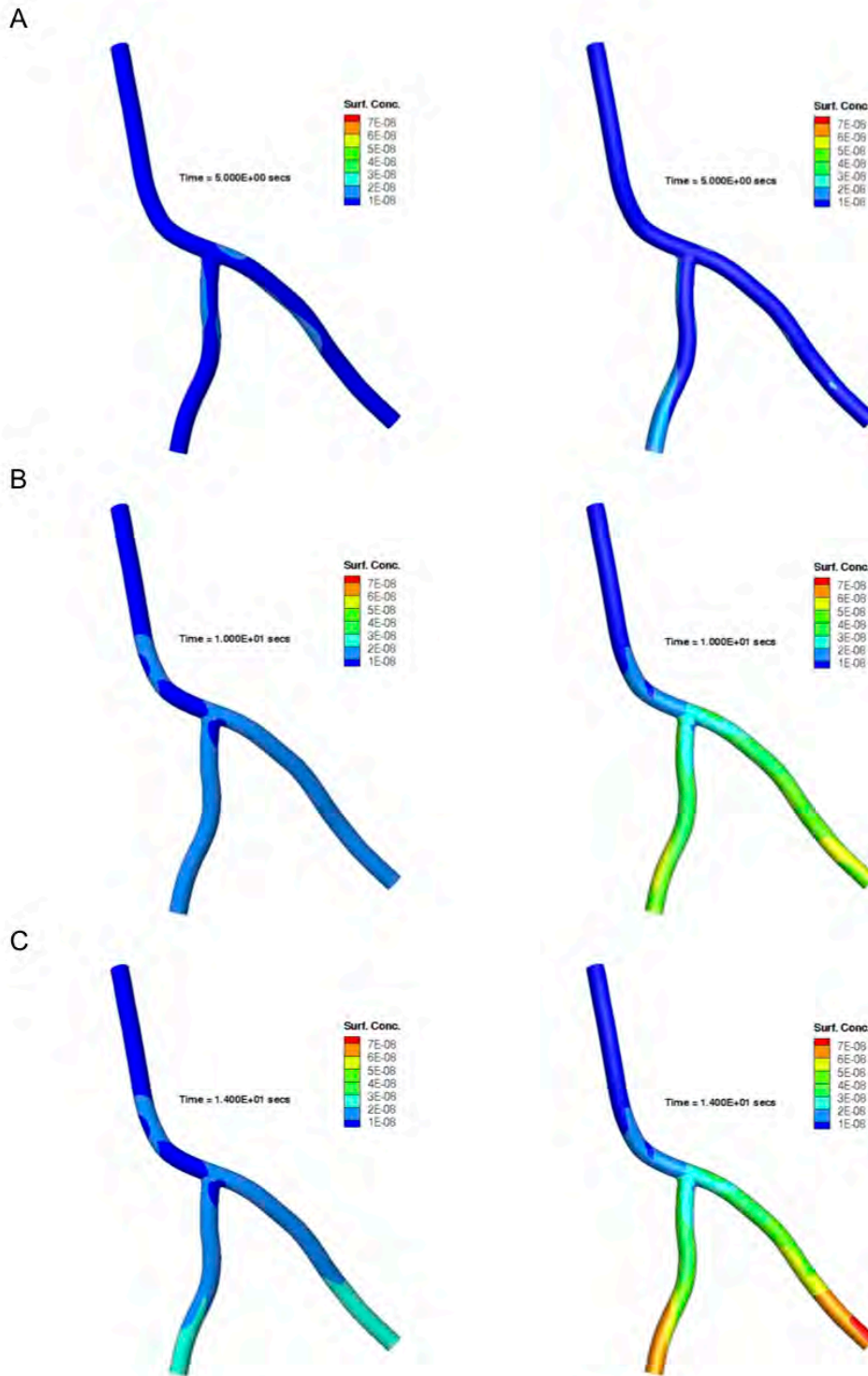


**Figure 4. Nanoparticle adhesion to the vessel walls: effect of nanoparticle size.** The normalized surface density of adhering nanoparticles is plotted along the arterial tree at various times  $t$  post injection, namely (A)  $t = 5$  s, (B)  $t = 10$  s and (C)  $t = 14$  s. The left and right columns present *in silico* data for the 0.5 and 2.0  $\mu\text{m}$  particle, respectively, in terms of particle number per unit area normalized by the injected dose [ $\text{cm}^{-2}$ ].

values of  $S$ , as those experienced in the LAD, the 0.5  $\mu\text{m}$  adhere more effectively than the 2  $\mu\text{m}$  particles, in agreement with what is shown in Figure 4 (see also Supplementary Figure 2: at  $S = 500 \text{ s}^{-1}$ ,  $\Pi \approx 0 \text{ mm/s}$  for the 2  $\mu\text{m}$  particles, and  $\Pi \approx 0.5 \times 10^{-7} \text{ mm/s}$  for the 0.5  $\mu\text{m}$  particles). Incidentally, these observations are consistent with those reported in the literature where it has been shown that low and oscillating  $S$  zones are associated with enhanced deposition and uptake of lipoprotein (LDL), and correlate well with atherosclerotic regions<sup>39-43</sup>. Because of the pulsatile nature of blood flow in the coronaries, the associated complex flow features create recirculation zones near the bifurcation resulting in alternate areas of high and low  $S$  levels (Supplementary Figures 5c, d). It should also be noted that the injection flow rate from the catheter can significantly alter the wall shear rate distribution and thus affect the particle deposition rates and patterns.

Second, the branching angle between the LAD and LCX was increased from  $76.8^\circ$  to  $106.8^\circ$ , in the same patient-specific coronary geometry. As expected, the velocity magnitude and the wall shear rate distribution are significantly affected by such a change<sup>44</sup>. While the flow features appear similar in the LCA, the velocity magnitude and distribution become noticeably different as the branching point is approached, and moving downstream towards the two outlets (Supplementary Figure 5). First, a larger recirculation area is seen at the branching. Second, due to the sharper bend encountered as the blood flows from the LCA to the LAD, a higher  $S$  zone appears at the LCA-LAD junction. Finally, the flow patterns in the LAD and LCX are different, introducing an asymmetry in the vascular tree. This difference is more noticeable in the post catheter injection period. As a consequence of the change in the  $S$  distribution, particles were observed to adhere more at the walls of the LAD rather than in the LCX. For both particle sizes, this is shown in Figure 5 and additional details are provided in Supplementary Figure 6.

Third, the contribution of the over-expression of receptor molecules on particle vascular deposition is investigated. For this, the surface density  $m_r$  in the LAD is increased by a

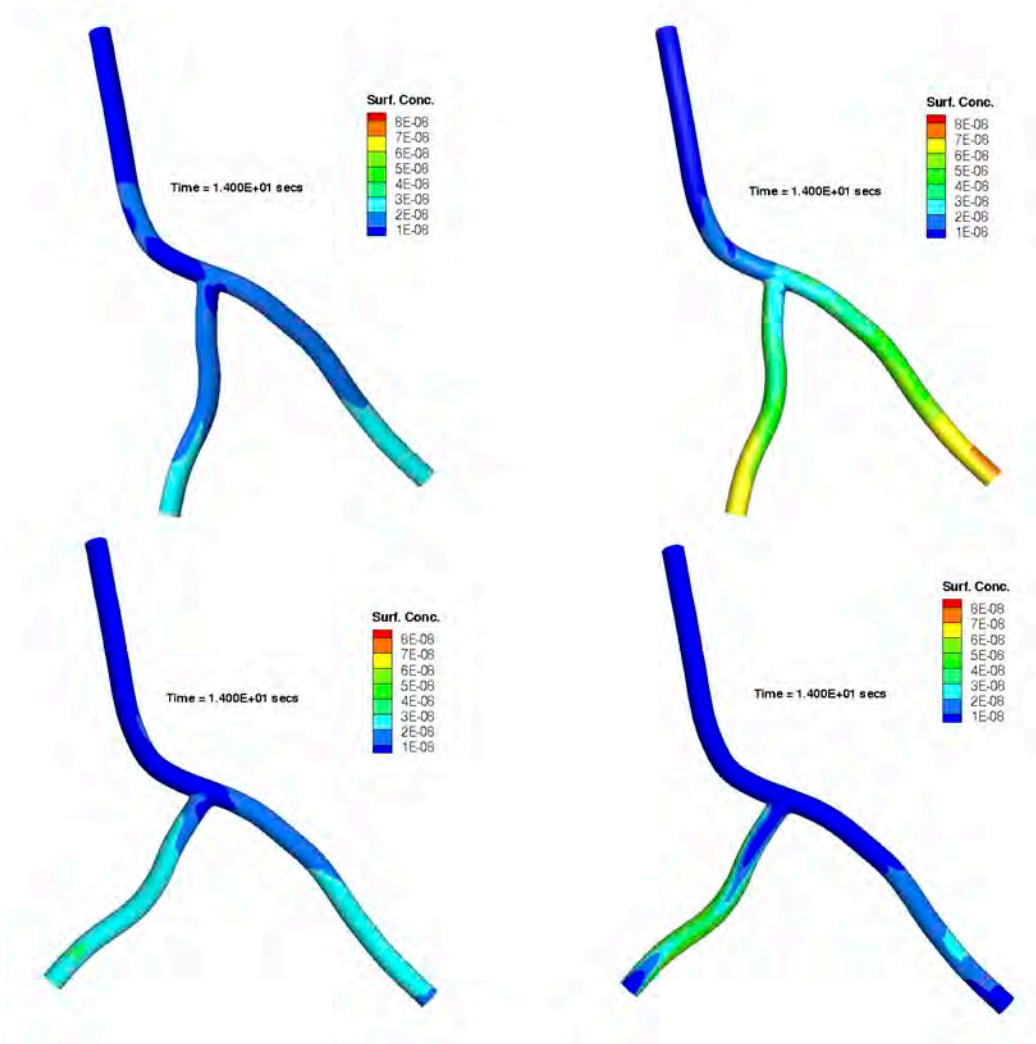


**Figure 5. Nanoparticle adhesion to the vessel walls: effect of vascular geometry.** The normalized surface density of adhering nanoparticles is plotted along the arterial tree at  $t = 14$  s, post injection. The left and right columns present *in silico* data for the 0.5 and 2.0  $\mu\text{m}$  particles, respectively. The top and bottom rows present *in silico* data for the smaller ( $76.8^\circ$ ) and larger ( $106.8^\circ$ ) branching angles, respectively. Data are presented in particle number per unit area normalized by the injected dose [ $\text{cm}^{-2}$ ].

factor of 10 compared to other regions in the vascular tree. A side-by-side comparison of the time evolution for the particle distribution is presented in Figure 6. Quite expectedly, particle concentration in the LAD is observed to be larger by almost an order of magnitude compared to the previous case, with no receptor over-expression. Note that the vascular deposition parameter  $\Pi$  grows almost linearly with  $m_r$ . Particle adhesion is considerably enhanced because of the greater receptor availability that promotes specific interaction and increases the likelihood of ligand-receptor bond formation. It is also very

interesting to observe that the increased receptor density tends to support a larger particle deposition within the recirculation zone as compared to other regions (Supplementary Figure 7).

The presented results demonstrate that the adhesion pattern of intravascularly injected particles follows the distribution of the wall shear rates and is therefore significantly affected by the vascular geometry. Larger particles (2.0  $\mu\text{m}$  in diameter) adhere more in the lower branches of the arterial tree, where the wall shear rates  $S$  are moderate ( $< 200 \text{ s}^{-1}$ ); whereas smaller particles (0.5  $\mu\text{m}$  in diameter) adhere more in the upper branches, where  $S$  is higher. It is also shown that as the branching angle in the arterial tree increases, the adhesion patterns become non-symmetric: patients with larger branching angles ( $\approx 106.8^\circ$ ) would receive more nanoparticles in the LAD than in the LCX. On the other hand, nanoparticles would distribute equally in the two arterial branches for patients with smaller branching angles ( $\approx 76.8^\circ$ ). Additionally, upregulation in the expression of vascular receptors is responsible for a non-symmetric and non-uniform vascular adhesion of the nanoparticles. These results clearly emphasize the importance of including patient-specific information for a proper selection of vascular delivery systems.

In the near future, the following scenarios can be envisioned where computational modeling and nanoparticle engineering would be intimately integrated. Currently, MRI and CT are the most easily accessible, minimally invasive systems for whole human body imaging and, in conjunction with ultrasonic measurements, can provide information on the three-dimensional architecture and velocity field in a patient-specific vasculature. Nanoparticles can be engineered as potent MRI, or CT, contrast agents (imaging nanoconstructs)<sup>45-48</sup>, molecularly targeted to a specific receptor family expressed over the diseased endothelial walls. This could be the integrin family on the tumor vasculature, inflammatory adhesion molecules in cardiovascular diseases and several others<sup>49</sup>. The number of adhering imaging nanoconstructs can be quantified by relating the contrast enhancement measured by the clinical scanner with the imaging properties of the single nanoconstruct. Knowing the number of adhering nanoparticles, the vascular geometry and mean hydrodynamic conditions, the computational model can be used to back

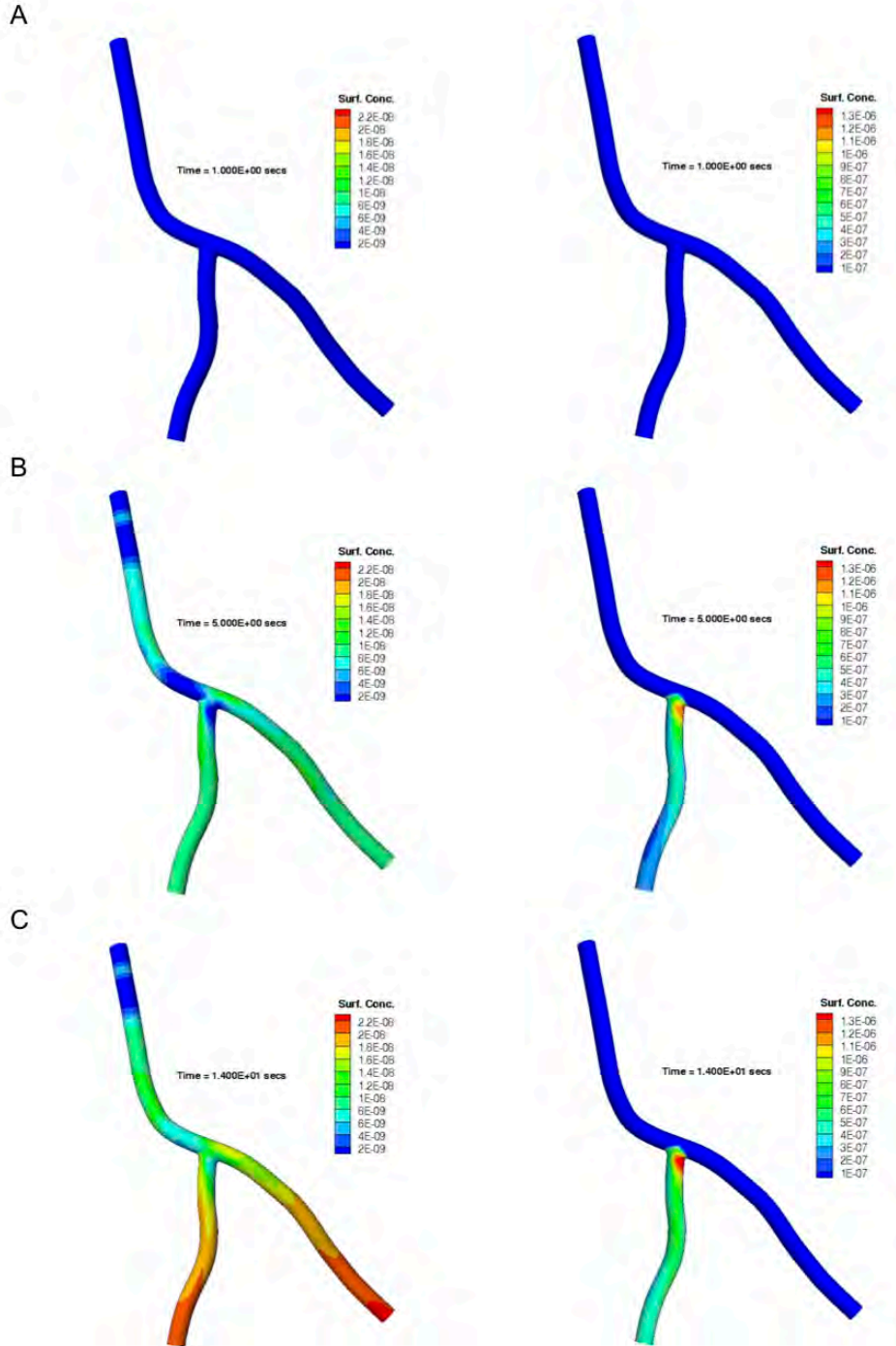


**Figure 6. Nanoparticle adhesion to the vessel walls: effect of surface density of vascular receptors.** The normalized surface density of  $0.5\ \mu\text{m}$  adhering nanoparticles is plotted along the arterial tree at various times  $t$  post injection: (A)  $t = 1\ \text{s}$ , (B)  $t = 5\ \text{s}$  and (C)  $t = 14\ \text{s}$ . Data are presented for a uniform receptor density ( $m_r = 10^9\ \text{\#}/\text{cm}^2$ ) along the vasculature (left column) and for an LAD receptor density 10 times larger than that in the LCA and LCX (right column). Note that the color map scales are different for the two cases and give the particle number per unit area normalized by the injected dose [ $\text{cm}^{-2}$ ].

calculate the mean receptor surface density following a reverse engineering approach. This would be extremely useful for the *in vivo* rapid screening of potential vascular targets in individual patients<sup>49</sup>. With all this information at hand, the optimal particle configuration, in terms of size, shape, surface and stiffness can be identified using the computational models with the objective of maximizing drug release at the target site while minimizing non-specific sequestration in healthy tissue. Indeed, these scenarios are within reach but can only be achieved with an orchestrated development of potent, safe nanoparticle-based imaging tools and accurate, efficient computational methods.

#### **ACKNOWLEDGMENTS**

This work was supported by the Cancer Prevention Research Institute of Texas through the grant CPRIT RP110262, and through the grants from the National Institutes of Health (USA) (NIH) U54CA143837 and U54CA151668. The additional support for MF from DoD/BCRP (W81XWH-09-1-0212) and the Ernest Cockrell Jr. Distinguished Endowed Chair, and that for TJRH from Portuguese CoLab Grant No. 04A are also gratefully acknowledged. The authors thank John A. Evans for his input and suggestions during numerical stabilization and Benjamin Urick from Texas Advanced Computing Center for his help with the artwork.

#### **AUTHOR CONTRIBUTIONS**

PD and SSH drafted the manuscript. SSH performed all the numerical implementation and calculations, developed the wall boundary condition and generated the figures; YZ helped in modifying the vascular geometry and writing the manuscript; XL helped in modifying the vascular geometry; FH provided input on the original draft and revision; MF provided input on the original draft and its revisions; TJRH developed the computational methodology, supervised the numerical simulations, and provided input on the original draft and its revisions; PD designed the “experimental plan”, and developed the wall boundary condition. All the authors discussed the results and commented on the manuscript.

## References

1. Weinshilboum R. Genomic medicine - Inheritance and drug response. *New England Journal of Medicine* 2003;348(6): 529-37.
2. Evans WE, McLeod HL. Drug therapy - Pharmacogenomics - Drug disposition, drug targets, and side effects. *New England Journal of Medicine* 2003;348(6): 538-49.
3. Kent DM, Hayward RA. Limitations of applying summary results of clinical trials to individual patients - The need for risk stratification. *Jama-Journal of the American Medical Association* 2007;298(10): 1209-12.
4. Ghosh S, Matsuoka Y, Asai Y, Hsin K-Y, Kitano H. Software for systems biology: from tools to integrated platforms. *Nat Rev Genet* 2011;12(12): 821-32.
5. Vizirianakis IS. Nanomedicine and personalized medicine toward the application of pharmacotyping in clinical practice to improve drug-delivery outcomes'. *Nanomedicine-Nanotechnology Biology and Medicine* 2011;7(1): 11-17.
6. Nie S. Nanotechnology for personalized and predictive medicine. *Nanomedicine : nanotechnology, biology, and medicine* 2006;2(4): 305.
7. Michor F, Liphardt J, Ferrari M, Widom J. What does physics have to do with cancer? *Nat Rev Cancer* 2011;11(9): 657-70.
8. Peer D, Karp JM, Hong S, Farokhzad OC, Margalit R, Langer R. Nanocarriers as an emerging platform for cancer therapy. *Nature Nanotechnology* 2007;2(12): 751-60.
9. Sutradhar A, Paulino GH, Miller MJ, Nguyen TH. Topological optimization for designing patient-specific large craniofacial segmental bone replacements. *Proceedings of the National Academy of Sciences of the United States of America* 2010;107(30): 13222-27.
10. Williams JM, Adewunmi A, Schek RM, et al. Bone tissue engineering using polycaprolactone scaffolds fabricated via selective laser sintering. *Biomaterials* 2005;26(23): 4817-27.
11. Hwang C-W, Wu D, Edelman ER. Physiological Transport Forces Govern Drug Distribution for Stent-Based Delivery. *Circulation* 2001;104(5): 600-05.
12. Migliavacca F, Dubini G. Computational modeling of vascular anastomoses. *Biomechanics and Modeling in Mechanobiology* 2005;3(4): 235-50.
13. Taylor CA, Hughes TJR, Zarins CK. Finite Element Modeling of Three-Dimensional Pulsatile Flow in the Abdominal Aorta: Relevance to Atherosclerosis. *Annals of Biomedical Engineering* 1998;26(6): 975-87.
14. Hossain SS, Hossain SFA, Bazilevs Y, Calo VM, Hughes TJR. Mathematical modeling of coupled drug and drug-encapsulated nanoparticle transport in patient-specific coronary artery walls. *Computational Mechanics* 2012;49(2): 213-42.
15. Deisboeck TS, Wang Z, Macklin P, Cristini V. Multiscale Cancer Modeling. *Annual Review of Biomedical Engineering* 2011;13(1): 127-55.
16. Swanson KR, Rockne RC, Claridge J, Chaplain MA, Alvord EC, Anderson AR. Quantifying the role of angiogenesis in malignant progression of gliomas: In silico modeling integrates imaging and histology. *Cancer Research* 2011.
17. Schoeberl B, Eichler-Jonsson C, Gilles ED, Muller G. Computational modeling of the dynamics of the MAP kinase cascade activated by surface and internalized EGF receptors. *Nature Biotechnology* 2002;20(4): 370-75.



18. Kim HJ, Vignon-Clementel IE, Coogan JS, Figueroa CA, Jansen KE, Taylor CA. Patient-Specific Modeling of Blood Flow and Pressure in Human Coronary Arteries. *Annals of Biomedical Engineering* 2010;38(10): 3195-209.
19. Torii R, Oshima M, Kobayashi T, Takagi K, Tezduyar TE. Fluid-structure interaction modeling of aneurysmal conditions with high and normal blood pressures. *Computational Mechanics* 2006;38(4-5): 482-90.
20. LaDisa JF, Guler I, Olson LE, et al. Three-dimensional computational fluid dynamics modeling of alterations in coronary wall shear stress produced by stent implantation. *Annals of Biomedical Engineering* 2003;31(8): 972-80.
21. Decuzzi P, Pasqualini R, Arap W, Ferrari M. Intravascular Delivery of Particulate Systems: Does Geometry Really Matter? *Pharmaceutical Research* 2009;26(1): 235-43.
22. Lee SY, Ferrari M, Decuzzi P. Design of bio-mimetic particles with enhanced vascular interaction. *Journal of Biomechanics* 2009;42(12): 1885-90.
23. van de Ven AL, Kim P, Haley OH, et al. Rapid tumorotropic accumulation of systemically injected plateloid particles and their biodistribution. *Journal of Controlled Release*(0).
24. Rolland JP, Maynor BW, Euliss LE, Exner AE, Denison GM, DeSimone JM. Direct fabrication and harvesting of monodisperse, shape-specific nanobiomaterials. *Journal of the American Chemical Society* 2005;127(28): 10096-100.
25. Chiappini C, Tasciotti E, Fakhoury JR, et al. Tailored Porous Silicon Microparticles: Fabrication and Properties. *Chemphyschem* 2010;11(5): 1029-35.
26. Champion JA, Katare YK, Mitragotri S. Making polymeric micro- and nanoparticles of complex shapes. *Proceedings of the National Academy of Sciences of the United States of America* 2007;104(29): 11901-04.
27. Acharya G, Shin CS, McDermott M, et al. The hydrogel template method for fabrication of homogeneous nano/microparticles. *Journal of Controlled Release* 2010;141(3): 314-19.
28. Zhang Y, Bazilevs Y, Goswami S, Bajaj CL, Hughes TJR. Patient-specific vascular NURBS modeling for isogeometric analysis of blood flow. *Computer Methods in Applied Mechanics and Engineering* 2007;196(29-30): 2943-59.
29. Hughes TJR, Cottrell JA, Bazilevs Y. Isogeometric analysis: CAD, finite elements, NURBS, exact geometry and mesh refinement. *Computer Methods in Applied Mechanics and Engineering* 2005;194(39-41): 4135-95.
30. Decuzzi P, Ferrari M. The adhesive strength of non-spherical particles mediated by specific interactions. *Biomaterials* 2006;27(30): 5307-14.
31. Bazilevs Y, Calo VM, Zhang Y, Hughes TJR. Isogeometric Fluid–structure Interaction Analysis with Applications to Arterial Blood Flow. *Computational Mechanics* 2006;38(4): 310-22.
32. Bazilevs Y, Calo VM, Cottrell JA, Hughes TJR, Reali A, Scovazzi G. Variational multiscale residual-based turbulence modeling for large eddy simulation of incompressible flows. *Computer Methods in Applied Mechanics and Engineering* 2007;197(1-4): 173-201.
33. Leuprecht A, Perktold K. Computer simulation of non-newtonian effects on blood flow in large arteries. *Computer methods in biomechanics and biomedical engineering* 2001;4(2): 149-63.

34. Taylor CA, Humphrey JD. Open problems in computational vascular biomechanics: Hemodynamics and arterial wall mechanics. *Computer Methods in Applied Mechanics and Engineering* 2009;198(45-46): 3514-23.
35. Olgac U, Poulidakos D, Saur SC, Alkadhi H, Kurtcuoglu V. Patient-specific three-dimensional simulation of LDL accumulation in a human left coronary artery in its healthy and atherosclerotic states. *American Journal of Physiology-Heart and Circulatory Physiology* 2009;296(6): H1969-H82.
36. Stangeby DK, Ethier CR. Computational Analysis of Coupled Blood-Wall Arterial LDL Transport. *Journal of Biomechanical Engineering* 2002;124(1): 1-8.
37. Matsuo S, Tsuruta M, Hayano M, et al. Phasic coronary-artery flow velocity determined by doppler flowmeter catheter in aortic-stenosis and aortic regulation. *American Journal of Cardiology* 1988;62(13): 917-22.
38. Johnston BM, Johnston PR, Corney S, Kilpatrick D. Non-Newtonian blood flow in human right coronary arteries: Transient simulations. *Journal of Biomechanics* 2006;39(6): 1116-28.
39. Gawaz M, Langer H, May AE. Platelets in inflammation and atherogenesis. *The Journal of Clinical Investigation* 2005;115(12): 3378-84.
40. Zarins CK, Giddens DP, Bharadvaj BK, Sottiurai VS, Mabon RF, Glagov S. Carotid bifurcation atherosclerosis. Quantitative correlation of plaque localization with flow velocity profiles and wall shear stress. *Circulation Research* 1983;53(4): 502-14.
41. Caro CG, Fitz-Gerald JM, Schroter RC. Atheroma and Arterial Wall Shear Observation, Correlation and Proposal of a Shear Dependent Mass Transfer Mechanism for Atherogenesis. *Proceedings of the Royal Society of London. Series B. Biological Sciences* 1971;177(1046): 109-33.
42. Feldman CL, Ilegbusi OJ, Hu Z, Nesto R, Waxman S, Stone PH. Determination of in vivo velocity and endothelial shear stress patterns with phasic flow in human coronary arteries: A methodology to predict progression of coronary atherosclerosis. *American Heart Journal* 2002;143(6): 931-39.
43. Ku D, Giddens D, Zarins C, Glagov S. Pulsatile flow and atherosclerosis in the human carotid bifurcation. Positive correlation between plaque location and low oscillating shear stress. *Arteriosclerosis, Thrombosis, and Vascular Biology* 1985;5(3): 293-302.
44. Perktold K, Peter RO, Resch M, Langs G. Pulsatile non-newtonian blood flow in three-dimensional carotid bifurcation models: a numerical study of flow phenomena under different bifurcation angles. *Journal of Biomedical Engineering* 1991;13(6): 507-15.
45. Winter PM, Caruthers SD, Kassner A, et al. Molecular Imaging of angiogenesis in nascent vx-2 rabbit tumors using a novel alpha(v)beta(3)-targeted nanoparticle and 1.5 tesla magnetic resonance imaging. *Cancer Research* 2003;63(18): 5838-43.
46. Chen W, Jarzyna PA, van Tilborg GAF, et al. RGD peptide functionalized and reconstituted high-density lipoprotein nanoparticles as a versatile and multimodal tumor targeting molecular imaging probe. *Faseb Journal* 2010;24(6): 1689-99.
47. Jokerst JV, Gambhir SS. Molecular Imaging with Theranostic Nanoparticles. *Accounts of Chemical Research* 2011;44(10): 1050-60.

48. Ananta JS, Godin B, Sethi R, et al. Geometrical confinement of gadolinium-based contrast agents in nanoporous particles enhances T(1) contrast. *Nature Nanotechnology* 2010;5(11): 815-21.
49. Staquicini FI, Cardo-Vila M, Kolonin MG, et al. Vascular ligand-receptor mapping by direct combinatorial selection in cancer patients. *Proceedings of the National Academy of Sciences* 2011;108(46): 18637-42.

## SUPPLEMENTARY MATERIALS

# ***in silico* Vascular Modeling for Personalized Nanoparticle Delivery**

S. S. Hossain, Y. Zhang, X. Liang, F. Hussain, M. Ferrari, T. J. R. Hughes, P. Decuzzi

**Parallel plate flow chamber experiments.** A parallel plate flow chamber system from GlycoTech Corporation was employed to study the particle transport and adhesion dynamics under controlled flow conditions (Supplementary Figure 1A). The flow chamber system comprises a PMMA flow deck, a silicon rubber gasket and a collagen-coated glass cover slip. Through silastic tubing, the inlet and outlet bores on the flow deck were connected to a syringe, mounted on a pump (Harvard Apparatus, MA), and to the waste, respectively. The syringe pump allowed for an accurate control of the flow rate in the chamber. The parallel plate flow chamber system was placed on the stage of a Nikon Ti-Eclipse epi-fluorescence inverted microscope. The cover slip was coated with collagen. Briefly, the cover slip was first cleaned in a petri dish with 70% Ethanol, and then exposed to a collagen solution (Sigma C8919, Type 1) obtained from calf skin at a concentration of about  $50 \mu\text{g}/\text{cm}^2$ . After about 5 h at room temperature, the cover slip was rinsed with PBS and left to dry under a biological hood. The silicon rubber gasket, which defines the dimensions of the channel, had a thickness of 0.274 mm, a length of 20 mm and a width of 10 mm. By controlling the volumetric flow rate with the syringe pump and the geometry of the chamber, wall shear rates  $S$  of 10, 75 and  $200 \text{ s}^{-1}$  were generated. Spherical fluorescent particles of different sizes (Fluoresbrite® YG Microspheres) were used, with a nominal diameter of 0.75, 3.0 and  $6.0 \mu\text{m}$ . The actual diameter was  $d_p = 0.720, 0.4899$  and  $6.596 \mu\text{m}$ . The particles were injected in the parallel plate flow chamber using the syringe pump. The dynamics of the particles under flow was monitored using dry microscope objectives at different magnifications, 10x, 20x and 40x. Images within the region of interest ( $658 \times 496$  pixel) were captured with an acquisition rate as high as possible, in relation with the exposure time required to capture the fluorescent particles. The resulting images were analyzed to quantify the number of

particles adhering over the substrate. Data were presented in terms of number of adhering particles ( $n_{adh}$ ) per unit area ( $A$ ) normalized by the total number of injected particles ( $n_{inj}$ ). Particles were dispersed in a Millipore water solution and counted using a Multisizer 4 Coulter Particle Counter (Beckman Coulter). Before each experiment, the particle solution was sonicated for 5 minutes to prevent the formation of aggregates.

**Governing equations for the particle transport and adhesion in a parallel plate flow chamber.** The Supplementary Figure 1B depicts the problem setup, which resembles the geometry of a parallel plate flow chamber: a channel with a rectangular cross section of 20 mm length ( $L$ ). As the width of the channel ( $b = 10$  mm) is substantially larger than the height ( $h = 0.274$  mm), a purely 2D analysis was considered. For a fully developed flow, the velocity profile within the channel is parabolic, such that

$$u_z = \frac{3Q}{2h} \left(1 - \frac{4y^2}{h^2}\right), \quad \text{and } u_x = u_y = 0. \quad (\text{S1})$$

Here,  $Q$  is the flow rate per unit channel width with the velocity components  $u_x$ ,  $u_y$  and  $u_z$  in the  $x$ ,  $y$  and  $z$  directions, respectively. Consequently, the wall shear rate  $S$  is uniform throughout the channel and has the form

$$S = \left. \frac{\partial u}{\partial y} \right|_s = \left. \frac{\partial u}{\partial y} \right|_{y=\pm h/2} = \frac{6Q}{h^2} \quad (\text{S2})$$

For the particle transport in the rectangular chamber, the governing equation Eq.(7) can be written explicitly as:

$$\frac{\partial C}{\partial t} = D \left( \frac{\partial^2 C}{\partial x^2} + \frac{\partial^2 C}{\partial y^2} + \frac{\partial^2 C}{\partial z^2} \right) - \left( u_z \frac{\partial C}{\partial z} \right) \quad (\text{S3})$$

where  $D$  is the particle isotropic diffusivity defined in Eq.(13). Note that  $\sigma$  was set to zero in that no reaction occurs in the flow domain. Eq.(S3) is subjected to the following initial and boundary conditions. Particles were released into the fluid stream at the center of the inlet surface for a time period of  $t_i = 30$  seconds. Hence, at the inlet boundary, for  $t < t_i$

$$\begin{aligned} C|_{\text{in}} &= C^0 \text{ at } y \leq \pm \frac{y_c}{2} \\ &= 0 \text{ elsewhere} \end{aligned} \quad (\text{S4})$$

where,  $y_c$  is the height of the area of injection; and at all other times

$$C|_{\text{in}} = 0 \quad (\text{S5})$$

At the channel outlet, a zero flux boundary condition was prescribed

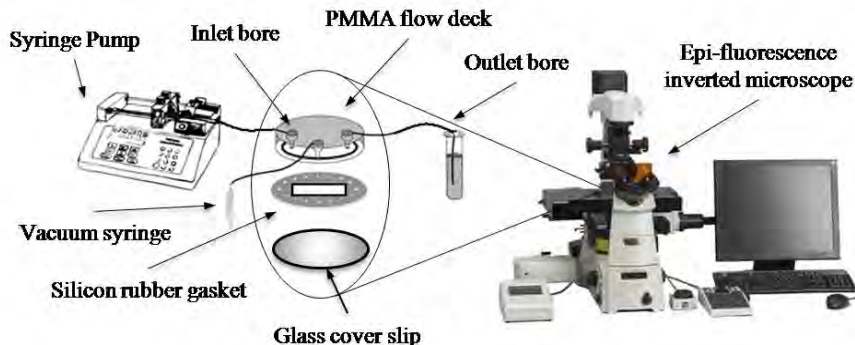
$$\left. \frac{\partial C}{\partial z} \right|_{\text{out}} = 0 \quad (\text{S6})$$

At the wall ( $y = \pm h/2$ ), following Eq.(18), the boundary condition on particle adhesion was imposed as

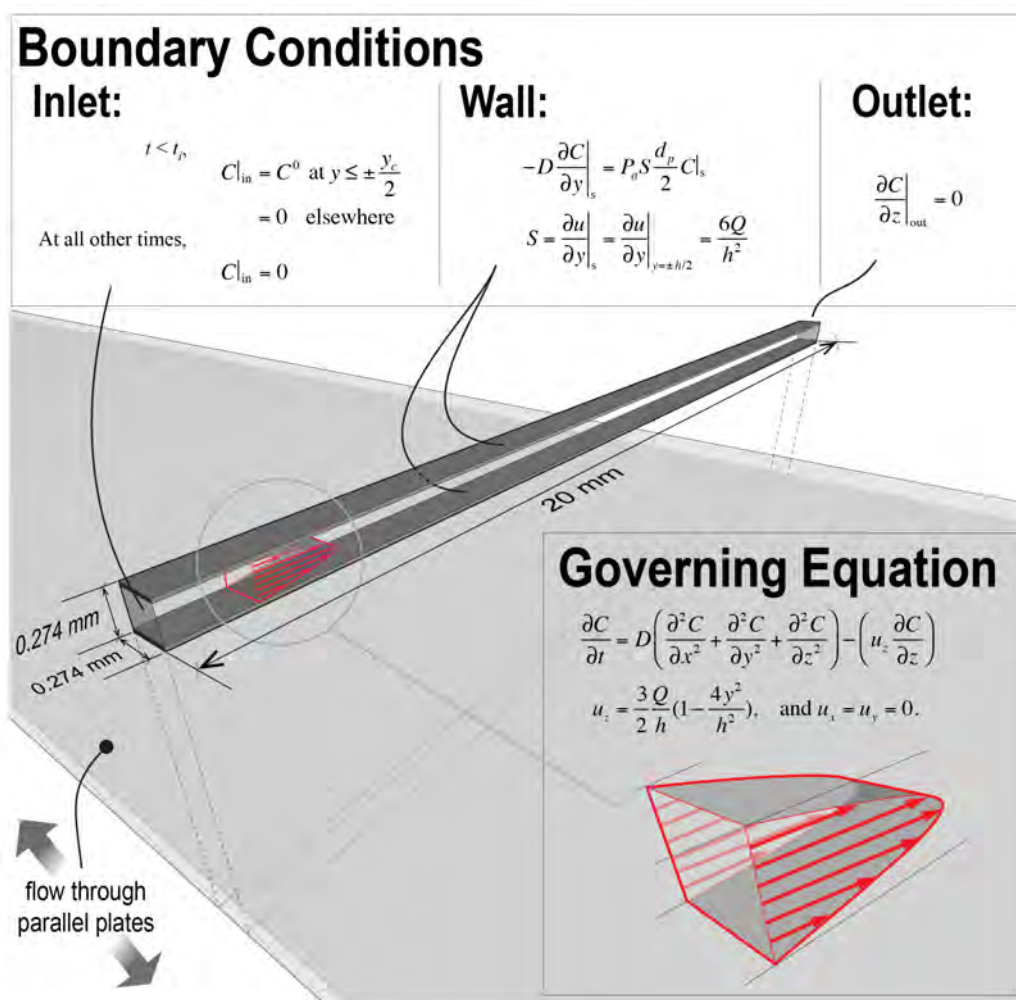
$$-D \left. \frac{\partial C}{\partial y} \right|_s = \frac{\partial \psi}{\partial t} = \Pi C|_s = P_a S \frac{d_p}{2} C|_s \quad (\text{S7})$$

Eqs.(S3)-(S7) were solved by applying Finite Element based Isogeometric Analysis<sup>1,2</sup> that uses NURBS to describe the geometry. Employing quadratic NURBS for the spatial discretization, a residual-based multiscale method<sup>3</sup> was implemented to solve the system of equations with the generalized- $\alpha$  method<sup>4,5</sup> for time advancement (readers are referred to the numerical procedures described in<sup>6</sup> for further details). The simulations were run with a time step of 0.05 s until all the particles left the fluid domain. A 77,824 element quadratic NURBS mesh with boundary layer refinement (higher resolution) was used to resolve the concentration boundary layers occurring near the wall and the inlet (i.e., to better capture the concentration gradients). Analyses run with a finer mesh and a greater number of time steps showed no observable differences in the solution. Particles of three different sizes with diameters  $d_p = 0.720, 4.899, \text{ and } 6.596 \mu\text{m}$  under three different wall shear rate cases, namely  $S = 10 \text{ s}^{-1}, 75 \text{ s}^{-1} \text{ and } 200 \text{ s}^{-1}$  were considered. In all three cases, the Péclet number was high ( $\text{Pe} \gg 1000$ ), making advection the dominant mode of particle transport rather than diffusion. To eliminate overshoot and undershoot near the inlet of the channel, the  $YZ\beta$  discontinuity capturing scheme<sup>7</sup> was employed.

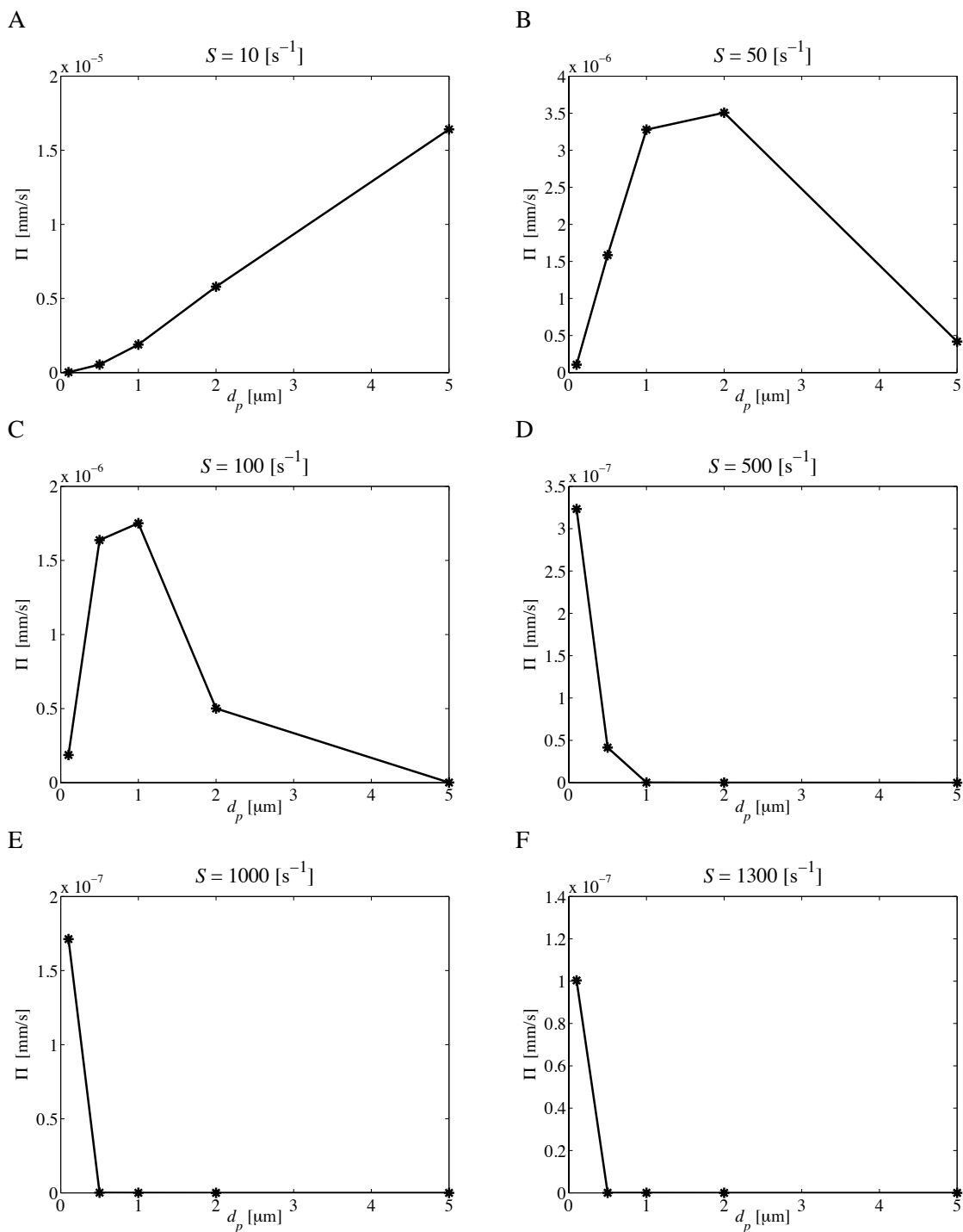
A



B

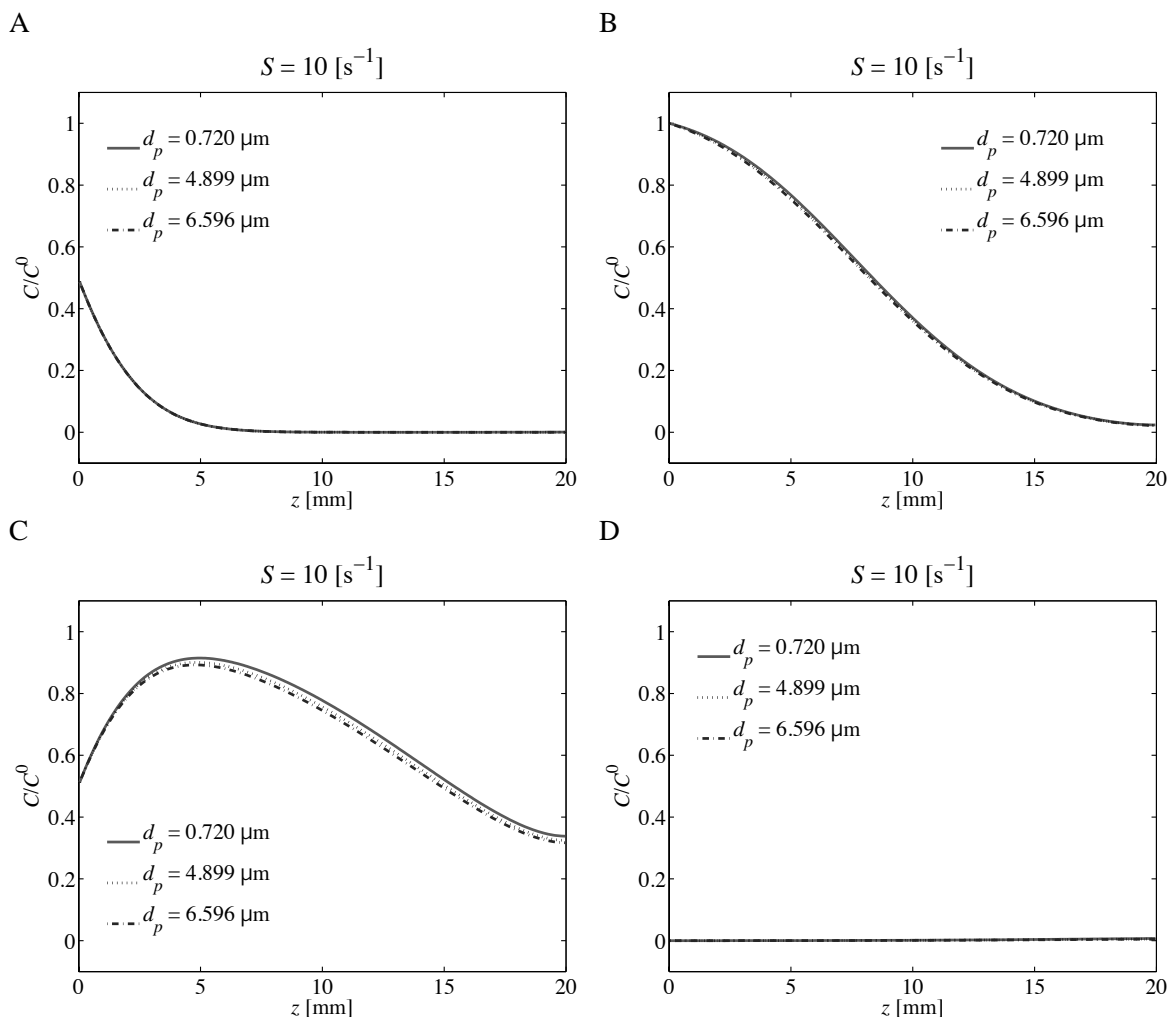


**Supplementary Figure 1. Transport and adhesion of nanoparticles in a parallel plate flow chamber (PPFC) apparatus.** (A) Schematic representation of the experimental system used for the *in vitro* experiments including an inverted epi-fluorescent microscope, a syringe pump and the PPFC. (B) Geometry and boundary conditions for the transport and adhesion problem specialized to the PPFC.

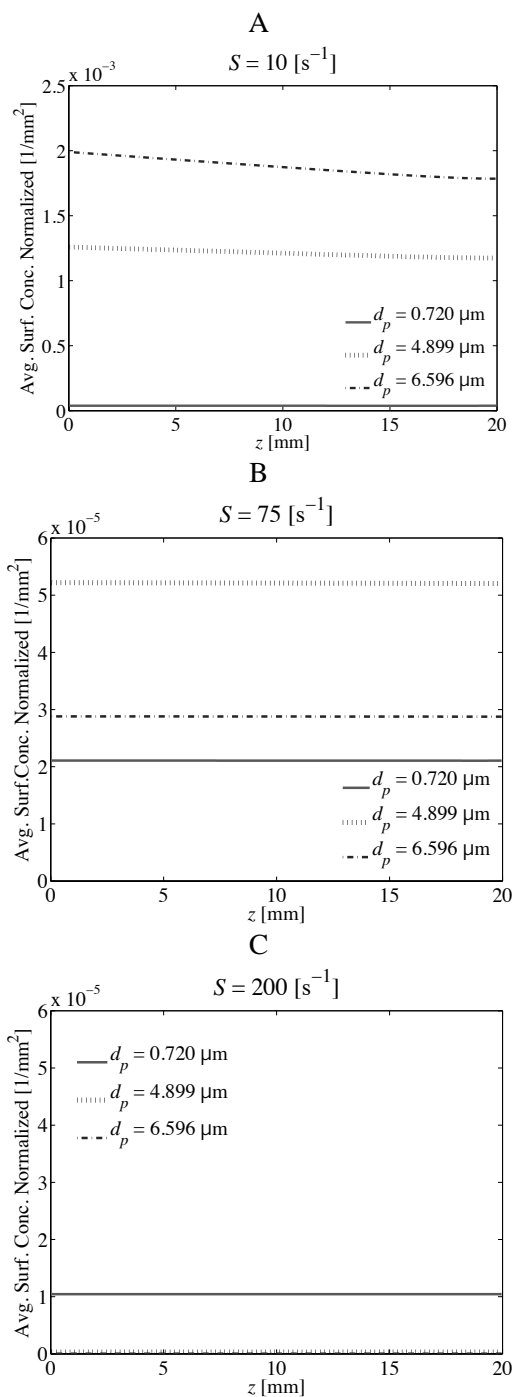


**Supplementary Figure 2. Vascular deposition parameter  $\Pi$ .** Variation of the vascular deposition parameter  $\Pi$  as a function of particle size  $d_p$  under different wall shear rates: (A)  $S = 10 \text{ s}^{-1}$ , (B)  $S = 50 \text{ s}^{-1}$ , (C)  $S = 100 \text{ s}^{-1}$ , (D)  $S = 500 \text{ s}^{-1}$ , (E)  $S = 1000 \text{ s}^{-1}$ , and (F)  $S = 1300 \text{ s}^{-1}$ .



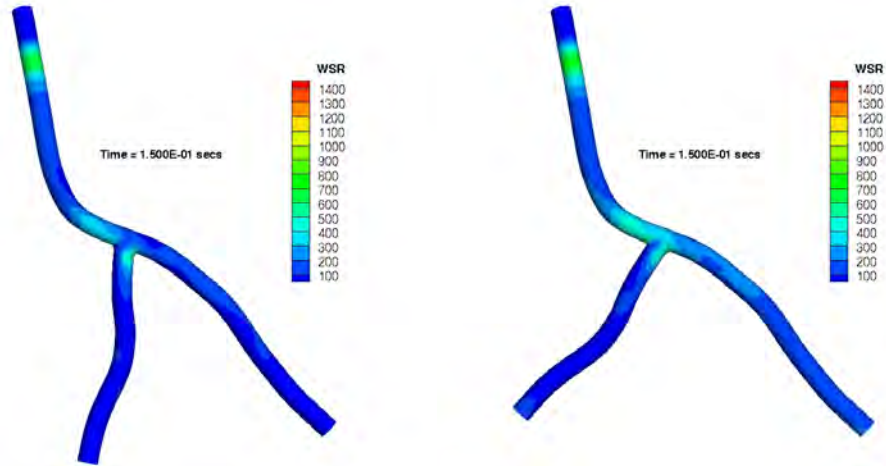


**Supplementary Figure 3. Variation of the wall volumetric concentration along the PPFC length.** Wall volumetric concentration  $C$ , normalized by the inlet volumetric concentration  $C^0$ , for different particle sizes under a shear rate of  $S = 10 \text{ s}^{-1}$  at (A)  $t = 5 \text{ s}$ , (B)  $t = 10 \text{ s}$ , (C)  $t = 35 \text{ s}$ , and (D)  $t = 138 \text{ s}$ . The coordinate  $z$  represents the distance from the inlet, along the channel length. The particle volumetric concentration  $C$  varies with time and location. At 138 s,  $C$  drops to zero meaning that all the injected particles have either adhered to the substrate or have left the chamber.

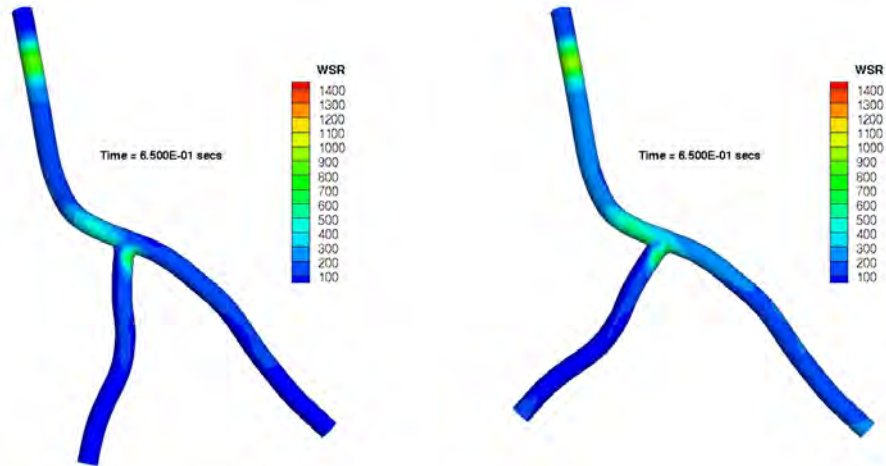


**Supplementary Figure 4. Average wall surface concentration of nanoparticles along the PPFC length.** The average surface concentration  $\psi$  of the particles depositing on the chamber substrate, computed over time and normalized by the number of injected particles  $n_{inj}$ , is plotted along the channel at the steady state (zero volumetric concentration in the chamber) under different hydrodynamic conditions: (A)  $S = 10 \text{ s}^{-1}$ , (B)  $S = 75 \text{ s}^{-1}$ , and (C)  $S = 200 \text{ s}^{-1}$ . The coordinate  $z$  represents the distance from the inlet, along the channel length.  $\psi$  is quite uniform along the channel and independent of the longitudinal coordinate  $z$ . Although a slight non-uniform distribution is observed at the lower shear rate ( $S = 10 \text{ s}^{-1}$ ), the  $\psi$  variation is still within 10%.

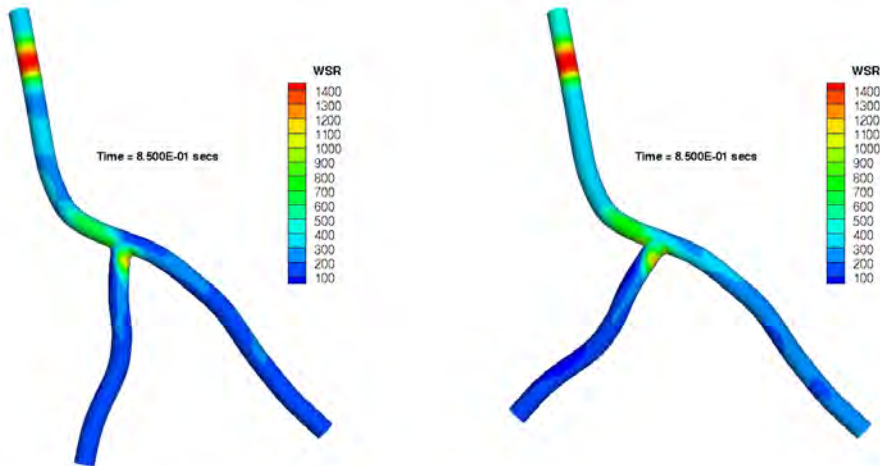
A



B

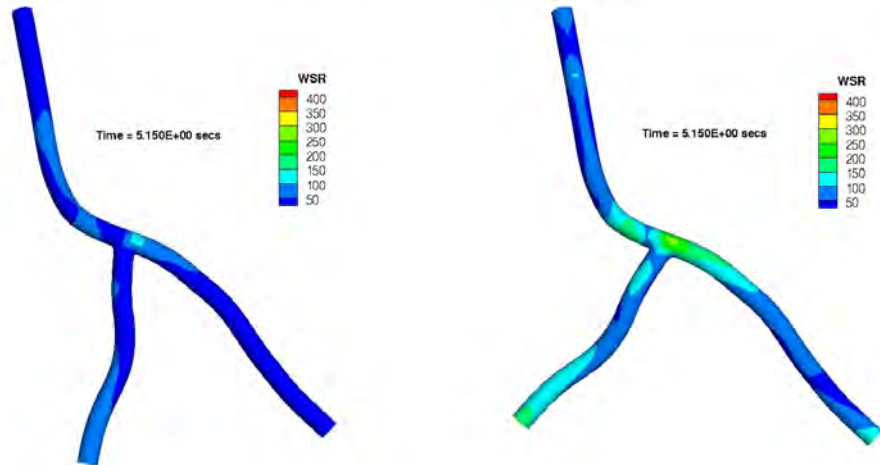


C

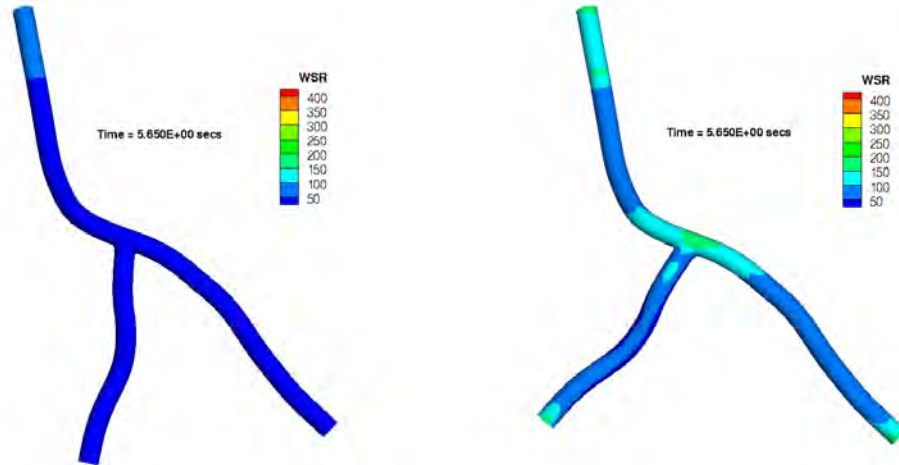


**Supplementary Figure 5a. Effect of the vascular geometry on the wall shear rate  $S$  (during continuous catheter infusion).** The spatial distribution of the wall shear rate  $S$  in  $s^{-1}$  for the two vascular geometries (branching angles of  $76.8^\circ$  and  $106.8^\circ$ ) at different times  $t$ , during the first second of catheter infusion.

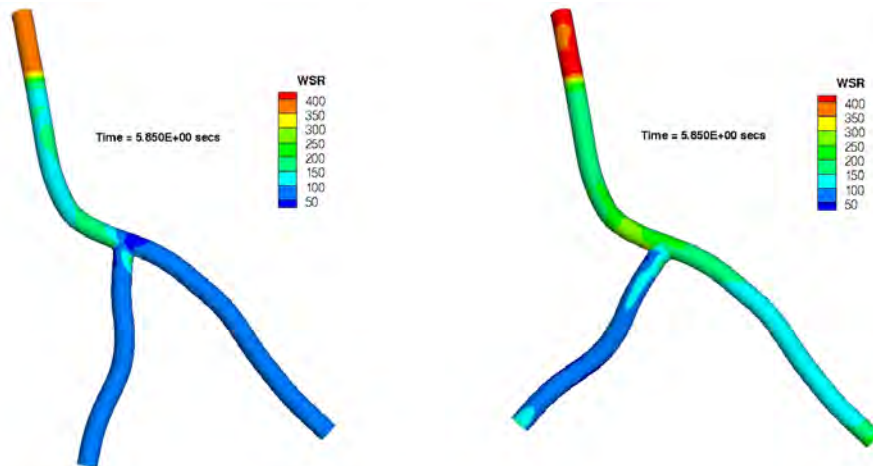
A



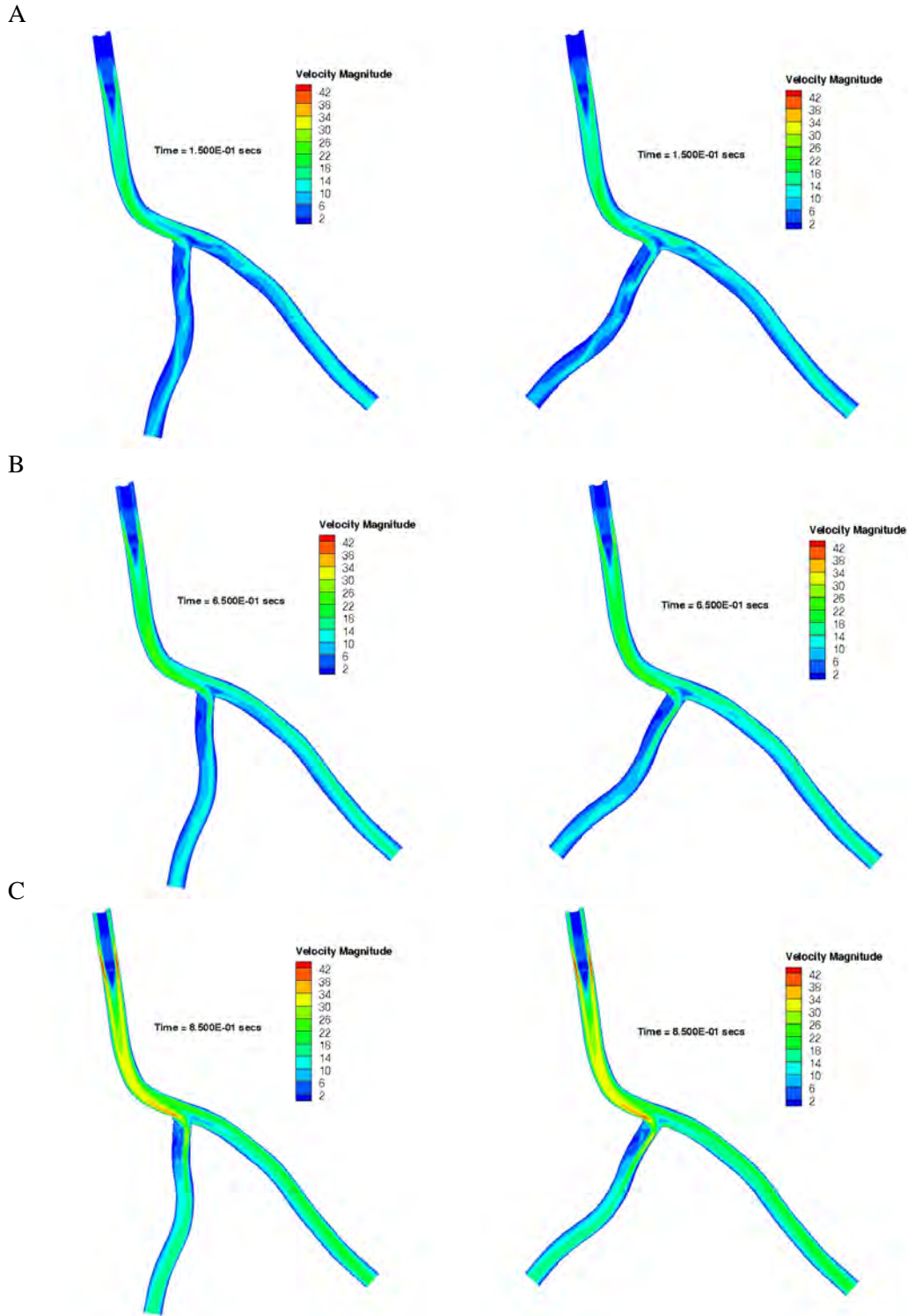
B



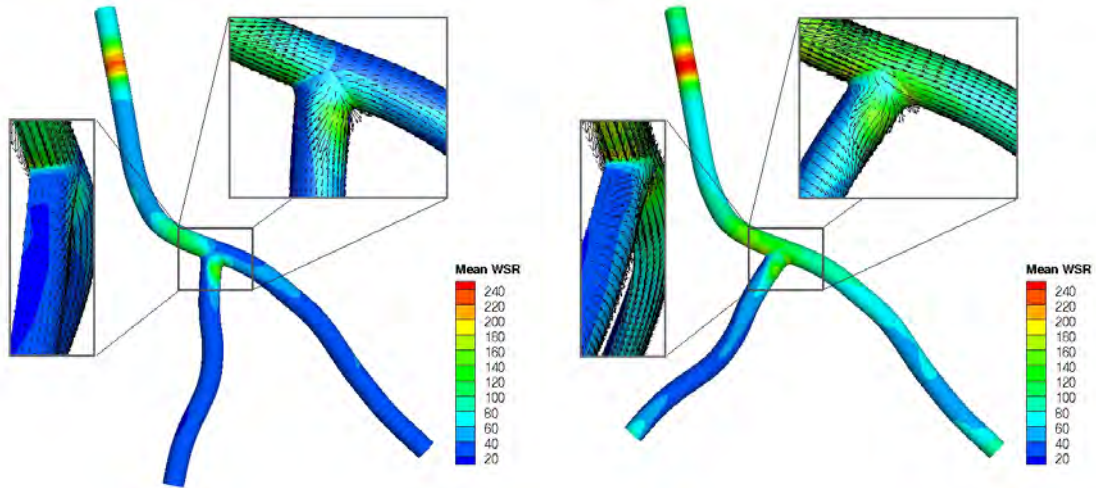
C



**Supplementary Figure 5b. Effect of the vascular geometry on the wall shear rate  $S$  (post catheter infusion).** The spatial distribution of the wall shear rate  $S$  in  $s^{-1}$  for the two vascular geometries (branching angles of  $76.8^\circ$  and  $106.8^\circ$ ) at different times  $t$ , during the first second post catheter infusion.

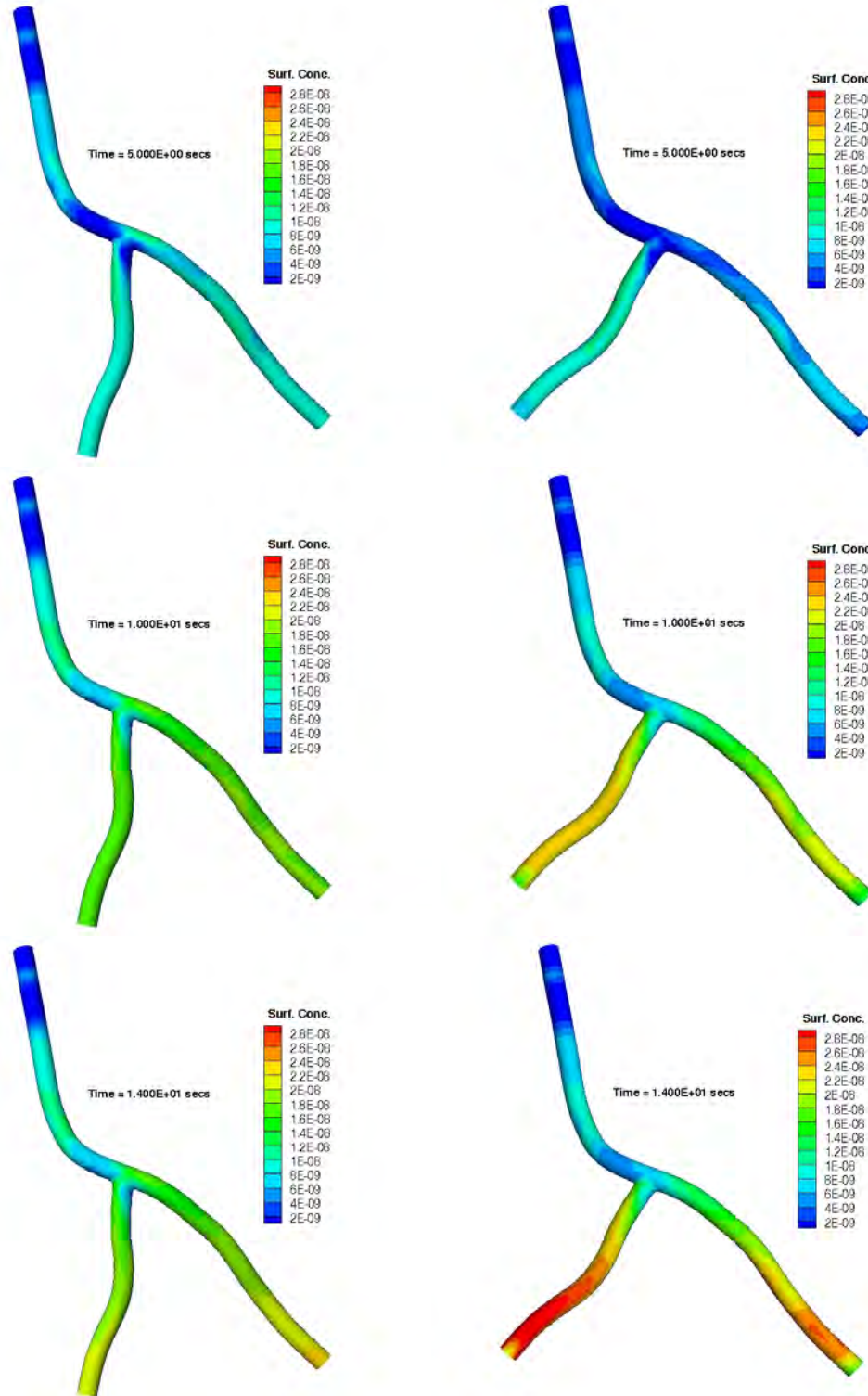


**Supplementary Figure 5c. Effect of the vascular geometry on the velocity distribution (during catheter infusion).** The velocity magnitude [cm/s] for the two vascular geometries (branching angles of 76.8° and 106.8°) at different times  $t$ , during the first second of catheter infusion.

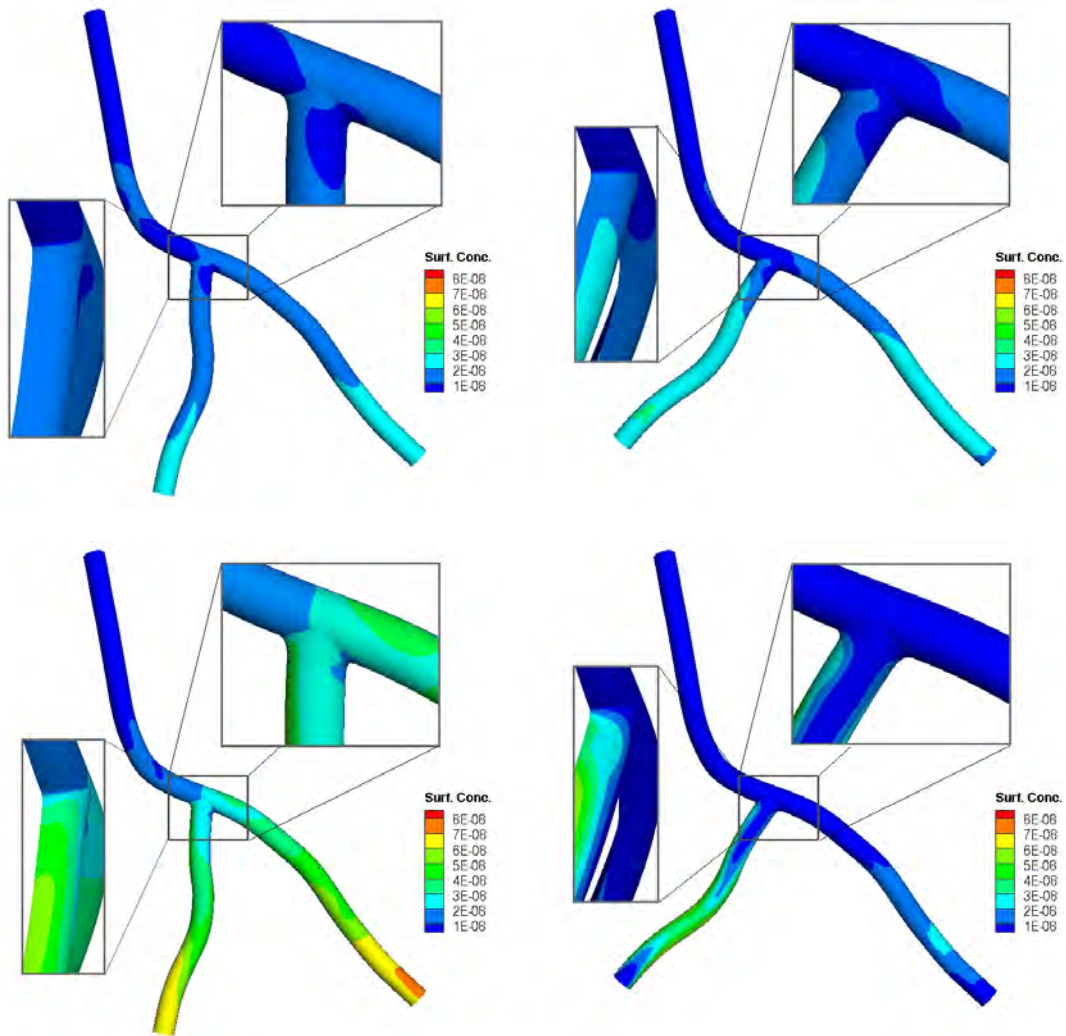


**Supplementary Figure 5d. Effect of the vascular geometry on the mean walls shear rate distribution (insight at the branching point).** The distribution of the mean wall shear rate  $S$  in  $s^{-1}$ , time averaged over the duration of simulation ( $= 14$  s), for the two vascular geometries (branching angles of  $76.8^\circ$  and  $106.8^\circ$ ). Insets highlight the recirculation zones with the corresponding vector representation (length of the arrow signifying the magnitude).



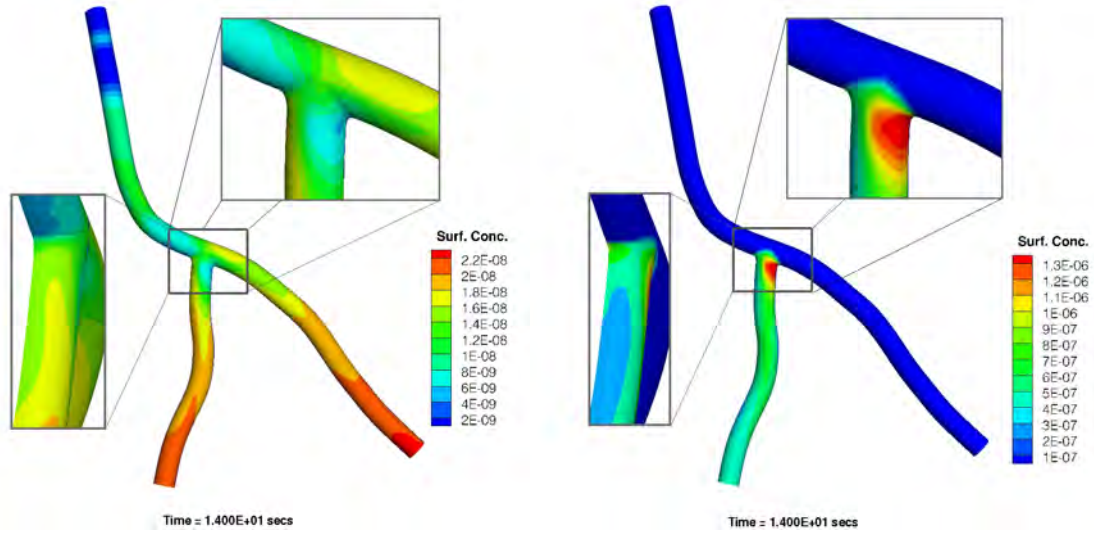


**Supplementary Figure 6a. Effect of the vascular geometry on surface particle adhesion (0.5  $\mu\text{m}$  particles).** Temporal and spatial distribution for the surface density of firmly adhering particle along the vascular tree. The surface concentration is normalized against the total number of particles injected [ $\text{cm}^{-2}$ ], for two vascular geometries (branching angles of 76.8° and 106.8°).



**Supplementary Figure 6b. Effect of the vascular geometry on surface particle adhesion at 14 s.** Spatial distribution for the surface density of firmly adhering particles along the vascular tree. The surface concentration is normalized against the total number of particles injected [ $\text{cm}^{-2}$ ], for two vascular geometries (branching angles of  $76.8^\circ$  and  $106.8^\circ$ ). Top row is for  $0.5 \mu\text{m}$  particles, whereas the bottom row is for  $2.0 \mu\text{m}$  particles. Insets highlight the distribution at the branch and within the recirculation zones.





**Supplementary Figure 7. Effect of the surface receptor density on particle adhesion.** The surface concentration of 0.5  $\mu\text{m}$  firmly adhering particles, normalized against the total number of particles injected [ $\text{cm}^{-2}$ ], is shown at  $t = 14$  s. Two cases are considered: uniform receptor density along the whole arterial tree (left); and 10 times higher receptor density in the LAD as compared to the LCA and LCX (right). Note that the color map scales are different for the two cases. Insets highlight the surface particle concentration at the branch and within the recirculation zones.

## **References**

1. Hossain SS, Hossainy SFA, Bazilevs Y, Calo VM, Hughes TJR. Mathematical modeling of coupled drug and drug-encapsulated nanoparticle transport in patient-specific coronary artery walls. *Computational Mechanics* 2012;49(2): 213-42.
2. Hughes TJR, Cottrell JA, Bazilevs Y. Isogeometric analysis: CAD, finite elements, NURBS, exact geometry and mesh refinement. *Computer Methods in Applied Mechanics and Engineering* 2005;194(39-41): 4135-95.
3. Bazilevs Y, Calo VM, Cottrell JA, Hughes TJR, Reali A, Scovazzi G. Variational multiscale residual-based turbulence modeling for large eddy simulation of incompressible flows. *Computer Methods in Applied Mechanics and Engineering* 2007;197(1-4): 173-201.
4. Chung J, Hulbert GM. A time integration algorithm for structural dynamics with improved numerical dissipation: The generalized- method. *Journal of Applied Mechanics* 1993;60: 371–75.
5. Jansen KE, Whiting CH, Hulbert GM. A generalized-[alpha] method for integrating the filtered Navier-Stokes equations with a stabilized finite element method. *Computer Methods in Applied Mechanics and Engineering* 2000;190(3-4): 305-19.
6. Hossain SS. Mathematical Modeling of Coupled Drug and Drug-encapsulated Nanoparticle Transport in Patient-specific Coronary Artery Walls. Department of Mechanical Engineering, Austin: University of Texas at Austin, 2009.
7. Bazilevs Y, Calo VM, Tezduyar TE, Hughes TJR. YZbeta discontinuity capturing for advection-dominated processes with application to arterial drug delivery. *International Journal for Numerical Methods in Fluids* 2007;54(6-8): 593-608.